

Charge transfer dynamics in β and *meso* substituted DTE Porphyrins.

Gabriele Di Carlo,^{a*} Alessio Orbelli Biroli,^b Francesca Tessore,^a Stefano Caramori,^{c*} Laura Casarin,^b Roberto Argazzi,^c Aurelio Oriana,^d Giulio Cerullo,^d Carlo Alberto Bignozzi^c and Maddalena Pizzotti^a

^aDepartment of Chemistry, University of Milan, INSTM Research Unit, Via C. Golgi 19, 20133 Milano, Italy. E-mail: gabriele.dicarlo@unimi.it

^bInstitute of Molecular Sciences and Technologies of CNR (ISTM-CNR), Via Golgi 33, I-20133 Milano, Italy.

^cDepartment of Chemical and Pharmaceutical Sciences, University of Ferrara, Via L.Borsari 46, 44121 Ferrara, Italy.

^dIFN-CNR, Dipartimento di Fisica, Politecnico di Milano, Piazza Leonardo da Vinci 32 20133 Milano, Italy

ABSTRACT

Transient optical studies, at the nanosecond and femtosecond timescales, have been carried out on three structurally different porphyrin dyes to probe their charge transfer dynamics relevant to spectral sensitization and DSSC operation. Two of them, showing a β substitution pattern, were previously reported: ZnB bearing an ethynylphenyl cyanoacrylic acceptor group and ZnBT bearing an additional π -conjugated dithienylethylene (DTE) chromophore in the acceptor pendant. The new porphyrin ZnMT, showing a donor-acceptor system in 5,15-*meso* position and the DTE unit as well, is characterized by a smaller HOMO-LUMO energy gap and by more significant push-pull character which guarantees more intense and red-shifted absorption bands compared to β substituted dyes. Besides, the introduction of the DTE unit promotes a remarkable gain in spectral sensitization both in β and *meso* positions.

We have demonstrated that the population of the absorption manifold resulting from the presence of the additional DTE chromophore leads to charge separation on a time scale of ca. 200 fs, irrespective of either the *meso* or β substitution position, resulting in the generation of a long-lived charge separated state surviving for several microseconds after injection. Thus, dyes equipped with the DTE bridge display the ability to convert photons in the 450-550 nm range, where light harvesters with more common push-pull designs do not show optimal absorption. Further, we have confirmed that β substitution may represent an effective strategy to combine extended spectral sensitization and optimal charge transfer rates with a synthetic and up-scalable feasibility.

INTRODUCTION

The growing interest in reducing greenhouse gases together with the ever increasing energy demand

for human activities makes the photovoltaic (PV) technology one of the most significant chances to obtain clean energy from renewable resources. To date, several PV technologies have been developed and reached excellent conversion efficiencies,¹⁻⁴ which are mandatory in case of limited space as for rooftop installations. On the other hand, when the PV modules have to be applied in Building Integrated Photo-Voltaic technology (BIPV) such as windows, skylights or façades, they can rely on larger active areas and lower conversion efficiencies may be considered acceptable. Nevertheless, this kind of application may involve numerous and sizable PV modules per building unit, requiring a large scale production and, as a consequence, low-cost manufacturing processes of such devices. Furthermore, characteristics as color, transparency, and long-term stability must be taken into account for solar cells eligible to BIPV applications.⁵ Dye-Sensitized Solar Cells (DSSCs),⁶ which use the low-cost and transparent TiO₂ semiconductor, emerged as a viable option to produce BIPV modules on industrial scale. In particular, great attention has been recently given to the porphyrin-based DSSCs.^{7,8} The strong electronic absorption bands together with the light collection capability^{9,10} and the tunable electrochemical^{11,12} properties, attained by a judicious molecular design, make porphyrins very promising sensitizers for this purpose. Many studies have been conducted on designing new porphyrin-based dyes, with the goal to maximize their PV performances or to tune the photoelectrochemical characteristics, reaching, in some cases, remarkable conversion efficiencies.^{7,13,14} All the molecular engineering processes aimed to a rational tailoring of a porphyrin structure have an effect on the energy levels of its molecular orbitals and consequently on its electrochemical characteristics. By acting on the donating and withdrawing ability of the substituents, it is easy to tune the HOMO and the LUMO energy levels of a porphyrin dye¹⁵⁻¹⁸ resulting in the push-pull character alteration of the donor-acceptor system. This may affect the rate of electron transfer processes occurring on the electrolyte/Dye/TiO₂ interface by acting on both the excited state thermodynamics and electronic coupling for charge injection.¹⁹ It is well known that *meso* substituted porphyrin dyes bearing the donor and acceptor groups in 5,15-position show a more significant push-pull character than the analogous porphyrin dyes having a substitution pattern in β -position.^{16,20,21} However, though a higher directional electron transfer along the push-pull system may increase the electron injection rate from the dye to the semiconductor, other factors must be considered. In a nanosecond time-resolved photophysical study comparing *meso* push-pull and β -pyrrolic substituted porphyrins, it was shown that the latter can rely on a superior shielding effect of the TiO₂ surface against charge recombination, providing better performances in DSSCs.²⁰ Moreover, in a series of *meso* substituted porphyrins designed to increase their push-pull character other factors such as the dye-loading on TiO₂, aggregation processes and non-optimal driving force for an activationless charge injection contributed in determining the photoconversion efficiency of the dyes.²² The photon

collection ability of a dye plays an important role in DSSC performance as well; the elongation of π -conjugated acceptor systems on porphyrin molecules, in fact, gives rise to a better light-harvesting over a wide range of wavelengths, resulting in a panchromatic effect on Incident Photon-to-Current conversion Efficiency (IPCE) spectra and in an enhanced photocurrent of photoelectrochemical cells.²³⁻²⁵ However a great importance is given to the study of charge transfer processes occurring at the dye/semiconductor/electrolyte interface and in particular to the electron injection^{26,27} which is the primary event of the charge separation. Sunahara *et al.*²⁶ observed a correlation between electron injection yield (Φ_{inj}) of porphyrin dyes determined from the Transient Absorption (TA) kinetics and the maximum IPCE obtained from the DSSCs. On the contrary, Tachibana *et al.*²⁸ in a photophysical comparative study between porphyrins and the ruthenium-based dye N719 observed that the kinetics are ultrafast and multiexponential for all dyes and the differences in DSSC performances should be attributed to other mechanisms affecting the sensitizing efficiencies of these dyes. Thus, the correlation between electron injection efficiency and photoconversion efficiency of porphyrin sensitized photoelectrochemical cells is not fully clear. It's also not completely clear to which extent the push-pull character of a given porphyrin dye is related to its charge injection rate.

In order to contribute to clarify these points, herein we analyze the electronic properties and the charge transfer dynamics of three different porphyrin dyes, bearing at either the β or the *meso* position a π conjugated arm designed to enhance their spectral sensitivity. In particular, we focus the attention on the impact of the elongation of the acceptor pendant, based on the dithienylethylene (DTE) system, on the photophysical and photoelectrochemical characteristics of the resulting dyes.

To this aim, the following series (Chart 1) was considered: i) ZnB,²⁰ a tetrarylporphyrin substituted in β -position with a typical ethynylphenyl cyanoacrylic pendant; ii) ZnBT,²³ a panchromatic tetrarylporphyrin substituted in β -position with a pendant bearing the DTE unit; iii) ZnMT, a new panchromatic diarylporphyrin showing a push-pull system in 5,15-*meso* positions and bearing the DTE unit on the acceptor substituent. The information extracted from this investigation is expected to help the further rational design and tailoring of new and more efficient porphyrin dyes.

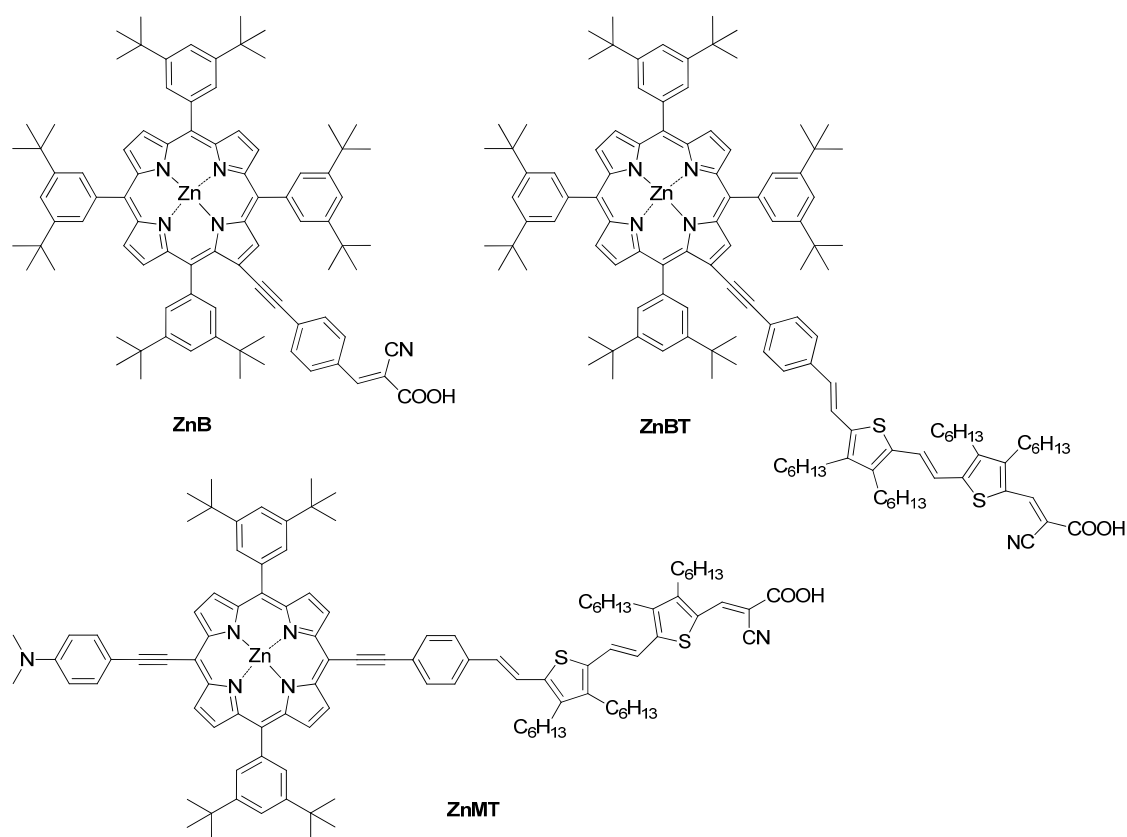


Chart 1: Molecular Structures of Porphyrin Dyes ZnB, ZnBT and ZnMT.

▪ Materials and Methods

Materials. All reagents and solvents used in the synthesis were purchased by Sigma-Aldrich and used as received, except Et₃N, Et₂NH (freshly distilled over KOH) and THF (freshly distilled from Na/benzophenone under nitrogen atmosphere). Silica gel for gravimetric chromatography (Geduran Si 60, 63–200 μm) and for flash chromatography (Geduran Si 60, 40–63 μm) were purchased by Merck. Glassware was flame-dried under vacuum before use when necessary. Microwave assisted reactions were performed using a Milestone MicroSYNTH instrument. ¹H-NMR spectra were recorded on a Bruker Avance DRX-400 and on a Bruker AMX 300 in THF-d₈ as solvent or CDCl₃ with addition, when necessary, of a drop of pyridine-d₅ (Cambridge Isotope Laboratories, Inc.). Electronic absorption spectra for the molar extinction coefficients calculation of all the dyes in THF were recorded using a Jasco V-530 spectrometer. Mass spectra were obtained with a VG Autospec M246 magnetic mass spectrometer with an LSIMS ionic source. Transparent semiconductor thin films on FTO substrates, intended for optical spectroscopy, were prepared by blade casting a nanocrystalline paste of TiO₂ (Dyesol DSL18NR-T), followed by drying and sintering at 450 °C for 45 min.

Synthesis of Porphyrin Dyes. ZnB²¹ and ZnBT²³ were prepared following the procedures previously reported. On the other hand, the synthesis of ZnMT with *meso* substitution pattern was performed by

a typical multistep approach (Scheme S1 in the Supporting Information). The diarylporphyrin intermediate **1**,²¹ bearing in 5,15 *meso* positions a 4-ethynyl-N,N-dimethylaniline and a 4-ethynylbenzaldehyde as substituents, and the phosphonate thienyl derivative **2**²³ were prepared as reported elsewhere. A Horner-Wadsworth-Emmons reaction between Porphyrin aldehyde **1** and the phosphonate **2** gave the porphyrin intermediate **3**. The latter was functionalized at the terminal thienyl unit by a Vilsmeier formylation leading to the aldehyde **4** which yielded the desired ZnMT product by a Knoevenagel condensation with cyanoacetic acid.

Computational Methodology. Density Functional Theory (DFT) and Time Dependent Density Functional Theory (TDDFT) calculations were performed for all the investigated Zn^{II} porphyrin dyes using the Gaussian 09 program package.²⁹ To reduce the computational overhead, the *tert*-butyl aryl substituents in ZnMT and ZnBT dyes were replaced by hydrogen atoms. The molecular structures were fully optimized *in vacuo* using the B3LYP³⁰⁻³² functional and a 6-311g* basis set.²¹ On the optimized structures, we performed single point calculations including solvation effects (THF) by means of a conductor-like polarizable continuum model (CPCM),³³ to compute orbital and transition energies and the associated electron density re-distribution maps (Electron Density difference Maps).

Electrochemical and Photoelectrochemical Investigation. The voltammetric studies were performed in a 4 cm³ cell, on 0.0005–0.001 M solutions in dimethylformamide (Aldrich, 99.8%) with 0.1 M tetrabutylammonium perchlorate (TBAP, Fluka) as the supporting electrolyte. In some cases sonication was applied to promote analyte dissolution. The solutions were deaerated by N₂ bubbling. The ohmic drop was compensated by the positive feedback technique.³⁴ The experiments were carried out using an AUTOLAB PGSTAT potentiostat (EcoChemie, The Netherlands) run by a PC with General-Purpose-Electrochemical-System (GPES) software. Cyclic voltammetry (CV) investigations were carried out at scan rates typically ranging from 0.05 to 2 V s⁻¹, with ohmic drop compensation; differential pulse voltammetry (DPV) curves (step potential: 5 mV, modulation amplitude: 50 mV) were also recorded for each compound as both oxidative and reductive scans. The working electrode was a glassy carbon disk one (AMEL, diameter = 1.5 mm) cleaned by synthetic diamond powder (Aldrich, diameter = 1 μm) on a wet cloth (STRUERS DP-NAP); the counter electrode was a platinum disk or wire; the operating reference electrode was an aqueous saturated calomel electrode, but the potentials ultimately referred to the Fc⁺/Fc couple (the intersolvental redox potential reference currently recommended by IUPAC^{35,36}), recording the CV pattern under the same working conditions. To prevent water and chloride leakage into the working solution a compartment filled with the operating medium and fitted with a porous frit was interposed between the reference electrode and the cell. JV curves of the solar cells were measured with the previously described PGSTAT electrochemical workstation under the white light generated by an ABET sun simulator equipped with

AM 1.5G filter. IPCE curves were acquired with a previously described custom made apparatus.²²

Preparation of DSSCs. FTO glass plates were washed in a detergent solution for 10 min and in 2-propanol for 10 min using an ultrasonic bath, then were heated at 450°C for 20 minutes.

The photoelectrodes were prepared by doctor blading, using (Dyesol 18NR-AO) paste which was diluted in some cases with terpineol in a 1:1.5 w/w ratio. The coated films were heated according to a programmed temperature ramp until reaching 500 °C, at which they stayed for 10 min before stopping heating and allowing the resulting films to cool down to room temperature.

Other electrodes were similarly prepared by using first a TiO₂ 18NR-T transparent paste and subsequently a layer of scattering TiO₂ paste (Solaronix), applied by doctor blading. After sintering, the electrodes were treated with 0.4 M TiCl₄ overnight and heated again at 450° for 30 minutes. Once cooled, the electrodes were immersed in a 0.2 mM solution of the dye, containing chenodeoxycholic acid 0.2 mM. Adsorption was carried out in the dark at different immersion times as described in the discussion section and the details are reported in the Supporting Information.

Solar cells were assembled with PEDOT counter electrodes using 25 μm thick hot-melt spacer (Surlyn, Dupont). Some cells were closed with paper clips without high-temperature sealing, in order to avoid thermal stress to the sensitizer. In other cells the polymer gasket was melt at 110 °C, and sealed with epoxy resin after inserting the electrolyte by vacuum backfilling.

The electrolyte used was: 0.6 M poly-methylimidazolium iodide, 0.2 or 0.02 M I₂, 0.1 M LiI, 0.05 M 4-tert-butylpyridine in acetonitrile.

Photophysical Measurements. Stationary UV–Vis spectroscopy was performed with an Agilent Cary 300 Spectrophotometer. Stationary emission spectroscopy was carried out with an Edinburgh Instruments FLS 920 Spectrofluorimeter equipped with a double emission monochromator. Spectral bandwidths of 2 nm were usually employed and the S/N ratio was optimized by summing 10 subsequent scans with 1 nm wavelength step. Spectra were corrected for the photomultiplier (R928P-Hamamatsu) response by using a factory built in calibration file. Emission lifetimes of the dyes in either diluted THF/EtOH solution or loaded onto the solid thin films were recorded with a PicoQuant PicoHarp 300 Time-Correlated Single Photon Counting (TCSPC) apparatus, by exciting at 460 nm (resonant with the Soret Band of the dyes) with a nanoled driven by a PDL 800 B pulsing unit (10 MHz, FWHM < 700ps).

Nanosecond Transient absorption (ns-TA) spectroscopy was performed with a previously described apparatus,³⁷ by using the 532 nm harmonic of a nanosecond Nd:YAG laser (Continuum Surelite II). When performing ns-TA on transparent thin films, the laser excitation fluence was reduced to ca. 2 mJ/cm²/pulse by using a defocusing plano-concave lens and various neutral density filters. A 532 nm notch filter prevented laser light from reaching the photomultiplier, whereas a 420 nm cut off filter

and a 50% T neutral density filter attenuated the white light probe beam and prevented direct TiO₂ excitation. From 10 to 30 laser shots, at a frequency of 0.2 Hz were averaged to reach a good S/N ratio. ns-TA measurements in the presence of iodide-based electron donor (0.6 M Allyl-Methyl Imidazolium iodide (AMII) + 0.1 M LiI in CH₃CN) were performed by drawing the electrolyte by capillarity inside the chamber (ca. 6–8 μm) constituted by a glass slide pressed against the TiO₂ photoanode. Thus, the negligible optical path allowed to avoid interferences originated by excitation of I₃⁻ created and accumulated at the interface during repeated measurements.

The dye regeneration efficiency was evaluated according to

$$\eta = \frac{k'_{reg}}{k'_{rec} + k'_{reg}}$$

where the two pseudo first order regeneration and recombination constants, k'_{reg} and k'_{rec} , were obtained by fitting the decay curve measured in the absence of the iodides in the electrolyte, and the one measured in the presence of iodides at the same concentration and composition used in the operating cell. Average pseudo-first order rate constants were calculated according to:

$$1/\tau_{avg} = K_{avg} = \left(\frac{(A_1 \tau_1^2 + A_2 \tau_2^2)}{(A_1 \tau_1 + A_2 \tau_2)} \right)^{-1}$$

Where A_1 and A_2 are the amplitudes of the of the fitting exponentials having time constants τ_1 and τ_2 respectively.

The femtosecond transient absorption (fs-TA) spectrometer starts with an amplified Ti:sapphire laser (Coherent Libra), generating 2-mJ, 100 fs pulses at 800 nm wavelength and 2-kHz repetition rate. A 300-μJ fraction of the pulse energy is used for the experiments, and is split into two beams. The first beam feeds an optical parametric amplifier, generating tunable pump pulses in the visible with ~70-fs duration; the second beam is focused in a CaF₂ crystal, generating a broadband white-light continuum (WLC) spanning the visible range (370-750 nm) and used as a probe. To avoid optical damage, the CaF₂ plate is slowly scanned in the beam focus. Pump and WLC probe pulses are non-collinearly focused on the sample and the transmitted probe, spatially selected by an iris, is sent to a silicon spectrometer capable of single-shot detection at the full 2-kHz repetition rate of the laser. The pump is modulated by a mechanical chopper at 1 kHz and the differential transmission spectra, defined as $\Delta T/T = (T_{pump\ on} - T_{pump\ off})/T_{pump\ off}$, are recorded as a function of probe wavelength and delay. Chirp-free $\Delta T/T$ maps are obtained by using a home-made dechirping algorithm. For the

experiments reported in the paper, the pump pulse was tuned to xxx nm and the used excitation fluences were in the xx-yy $\mu\text{J}/\text{cm}^2$ range.

(Setting delle misure al femtosecondo???) (...CERULLO...)

▪ RESULT AND DISCUSSION

Spectral and Electronic properties.

The electronic properties of ZnB, ZnBT and ZnMT porphyrins have been investigated by CV. Patterns were measured at 0.2 V s^{-1} on the GC electrode in DMF + 0.1 M TBAP and results are summarized in Table 1. The electrochemical properties of ZnB²¹ and ZnBT²³ have already been fully investigated by some of us elsewhere. Here, we report the fundamental results for a better comparison with the new synthesized ZnMT porphyrin having a different substitution pattern with respect to the first ones. In particular, we focus our attention on differences in HOMO and LUMO energy levels and the resulting HOMO-LUMO gaps which are strictly related to the push-pull character of the systems.

In all cases more than one oxidation and reduction peak can be observed in the available potential window, the first of them reversible or quasi reversible from both the electrochemical and chemical point of view, affording estimation of formal potentials $E^{\circ'} = (E_{\text{rev,forward}} + E_{\text{rev,backward}})/2$ (approaching standard potentials E° but neglecting activity coefficients). The availability of $E^{\circ'}$ parameters in turn affords the most reliable approach to the calculation of HOMO and LUMO energy levels:³⁸

$$E_{\text{LUMO}} (\text{eV}) = -e \times [(E^{\circ',1c}/V(\text{Fc}^+|\text{Fc}) + 4.8 \text{ V}(\text{Fc}^+|\text{Fc vs zero}))]$$

$$E_{\text{HOMO}} (\text{eV}) = -e \times [(E^{\circ',1a}/V(\text{Fc}^+|\text{Fc}) + 4.8 \text{ V}(\text{Fc}^+|\text{Fc vs zero}))]$$

resulting in the HOMO and LUMO energies and energy gaps E_g reported in Table 1.

Table 1. Key CV features and the electrochemical energy levels HOMO and LUMO derived therefrom.

Dye	$E^{\circ',1a}/V^a$ (Fc ⁺ Fc)	$E_{p,1a}/V^a$ (Fc ⁺ Fc)	$E_{p,1c}/V^a$ (Fc ⁺ Fc)	$E^{\circ',1c}/V^a$ (Fc ⁺ Fc)	HOMO/eV	LUMO/eV	$\Delta E^{\circ'}/V$ ($E_{g,EC}/\text{eV}$)
ZnB	0.32	0.35	-1.72	-1.69	-5.12	-3.11	2.02
ZnBT	0.36	0.39	-1.75	-1.70	-5.16	-3.10	2.06
ZnMT	0.21	0.25	-1.72	-1.63	-5.01	-3.17	1.84

^a $E^{\circ',1c}$ and $E^{\circ',1a}$ (or $E_{p,1c}$ and $E_{p,1a}$) all referred to the ferrocene couple.

Considering the structurally similar porphyrins having a β -substitution pattern, no significant differences can be noticed in the first reduction potentials (table 1) of ZnB (-1.69 V) and ZnBT (-1.70 V) due to the presence in both structures of the electron withdrawing cyanoacrylic group which provides the favourable reduction site. The *meso*-substituted ZnMT dye displays a first oxidation peak at a significantly less positive potential (0.21 V vs Fc/Fc⁺), due to the presence of the electron

donating dimethylamino donor group. The donor-acceptor system in *meso*-position can rely on a more efficient charge transfer character that strongly impacts on the first reduction potential as well, resulting in less negative value (-1.63 V) compared to ZnB and ZnBT. Consequently, the ZnMT porphyrin shows a narrower HOMO-LUMO energy gap ($E_g = 1.84$ eV) than the other two studied systems, as a result of an alteration on both the HOMO and LUMO energy levels, less negative and more negative respectively.

The experimental electrochemical levels are in good qualitative and quantitative agreement with the computed frontier energy levels (Figure 1). HOMOs of ZnB and ZnBT are found at -5.32 and -5.24 eV respectively, while the HOMO of ZnMT is found at -4.97 eV due to a substantial contribution by the amino donor (Table 2S). Computed LUMO energies of all dyes are very close to -3 eV, which agree within ca. 0.1 eV with the electrochemical results. Nevertheless, the fine variations in the electrochemical trend of reduction potentials are not reproduced by the calculation, showing the LUMOs of both DTE substituted dyes at energies marginally more negative (by -0.03 eV) than the ZnB species. In all cases LUMOs display a large density on the π conjugated bridge, involving the cyanoacrylic acceptor (Table 2S).

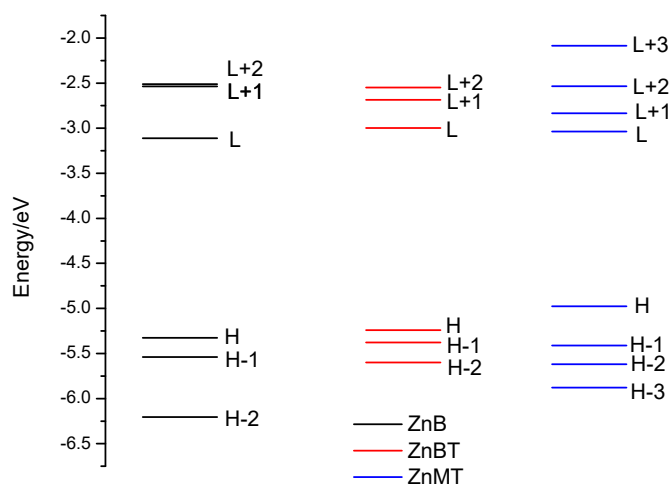


Figure 1. Computed Energy levels (vs vacuum) of the frontier orbitals of ZnB, ZnBT and ZnMT dyes. These orbitals contribute to the lowest singlet transitions in the 1.9-2.55 eV range.

The electronic absorption spectra of ZnB, ZnBT and ZnMT porphyrins in THF solution are reported in Figure 2. All spectra show the typical features of porphyrin molecules: an intense B band at around 450 nm and less intense Q bands at longer wavelengths. In particular the *meso*-substituted porphyrin ZnMT shows a single stronger Q band, at longer wavelengths (638 nm), compared to the β -substituted

porphyrins which show two less intense bands at 568 nm and 606 nm for ZnB, 566 nm and 603 nm for ZnBT. The red-shifted Q band of ZnMT is ascribed to the more significant push-pull character typical of the *meso* donor-acceptor system.

Noticeably, as previously reported,^{23, 24} the panchromatic porphyrins bearing the DTE unit in the acceptor pendant, ZnBT and ZnMT, are characterized by an additional broad and featureless absorption band around 500 nm, bridging the spectral portion uncovered by the lack of π delocalized thienyl moiety in the case of ZnB. Comparing the spectra of ZnB and ZnBT in solution, a slight blue-shift in the Q bands is observed in the latter, which we assign to the elongation of the π -system in the acceptor unit. Conversely, as will be discussed later, a remarkable red-shift of the same bands with respect to ZnB is observed when ZnBT is anchored to TiO₂ photoanodes .

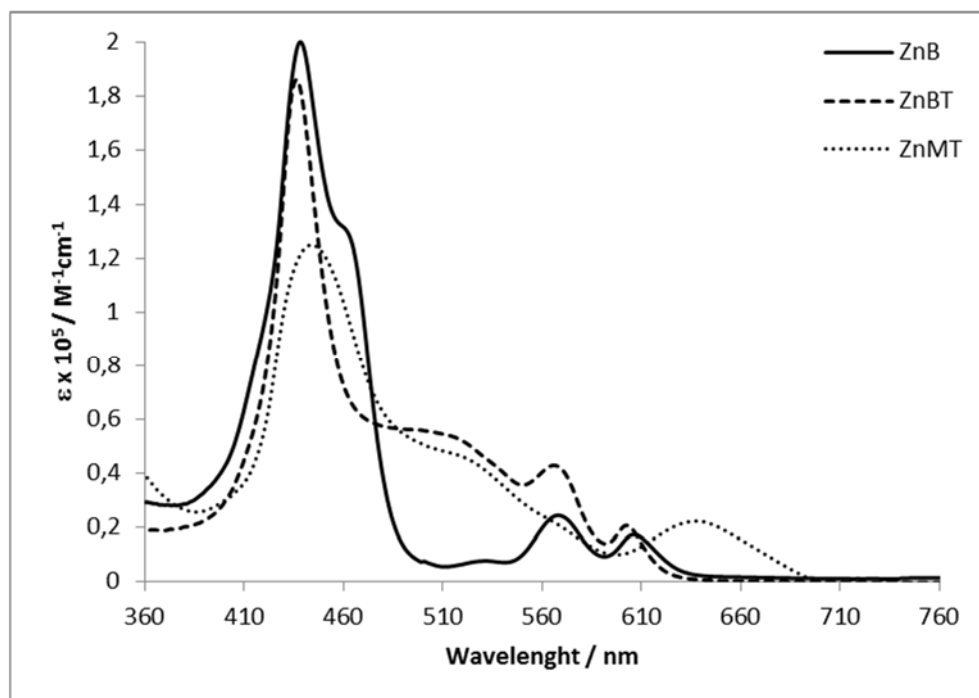
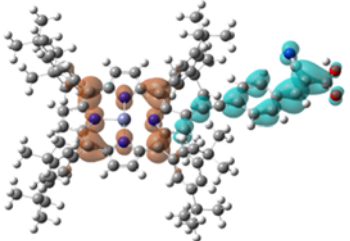
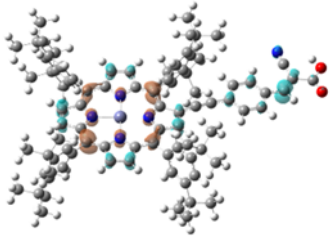
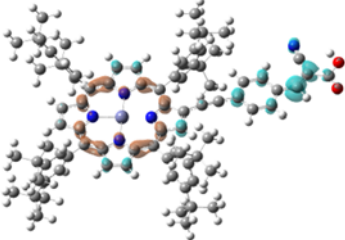
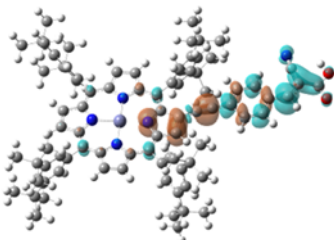
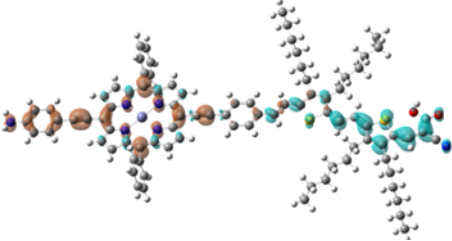
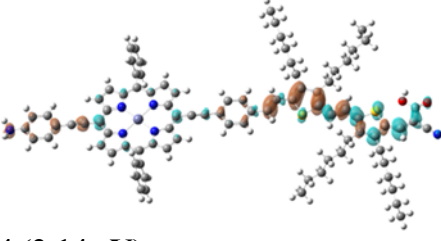
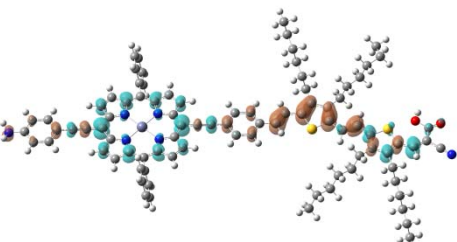
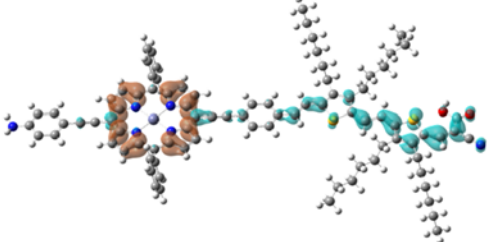


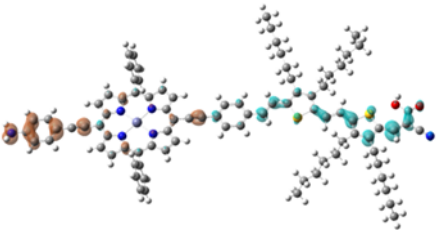
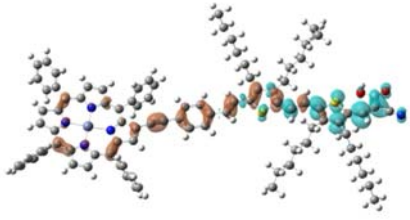
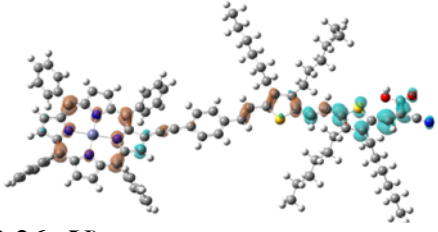
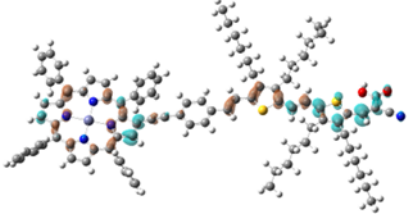
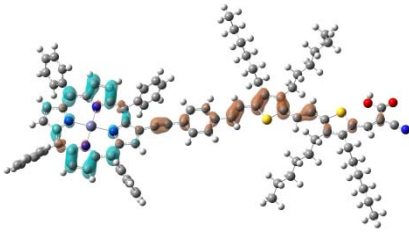
Figure 2. ϵ -normalized optical absorption spectra of ZnB, ZnBT and ZnMT in THF solution.

Generally, TDDFT calculations in THF afforded vertical transitions having a good agreement in energy with the experimental absorption spectra, with the lowest computed vertical excitation energies being lower than the experimental lowest Q band maximum by amounts varying between 0.1 eV (ZnBT) 0.13 eV (ZnB) and 0.25 eV (ZnMT) (Figure 1S and Table 1S). However, in the case of ZnBT and ZnMT, the oscillator strengths of the lowest transitions, having a dominating HOMO-LUMO character ($\geq 90\%$), are largely overestimated by the calculations, appearing as the most intense among all transitions under consideration. Nevertheless, vertical excitations to higher singlet states ($S_0 \rightarrow S_{n+1}$), reproduce the absorption manifold between the B and Q band with acceptable accuracy. In general the computed transitions are described by mixed contributions in the Kohn-Sham basis

involving excitation from the energy levels summarized in Figure 1 and in Table 1S. In order to gain a visualization of the change in molecular electronic density following optical excitation in terms of the intuitive concept of “holes” and “electrons”, electron density difference maps (EDDM) corresponding to selected optical transitions, depicted with a cut off threshold of 0.001, are reported in Table 2. Relevant to the photophysical study, the most intense optical transitions (i.e. with oscillator strength >0.09) populated by excitation of the absorption manifold between the B and Q band of the porphyrin sensitizers where considered. These are the states which should be first populated at the energies of the optical excitation pumps (i.e. from 2.53 to 2.33 eV) selected for the transient investigation and which resulted in electron injection into TiO₂.

Table 2. Electron Density Difference Maps and vertical transition energies from TDDFT B3LYP/6311G,d calculations. Orange: depleted electronic density; cyan: increased electronic density.

Dye	EDDM transition number (energy)		
ZnB	 1 (1.91 eV)	 3 (2.33 eV)	
	 4 (2.37 eV)	 5 (2.69 eV)	
	ZnMT	 1 (1.68 eV)	 4 (2.14 eV)
		 6 (2.46 eV)	 6 (2.46 eV)

	5 (2.36 eV)	
		
	7 (2.55 eV)	
ZnBT		
	1 (1.96 eV)	4 (2.26 eV)
		
	5 (2.36 eV)	7 (2.55 eV)

The EDDMS of the dye series under investigation confirm the strong charge transfer (CT) character of the excited states, where the bridge orbitals contribute actively to spatial delocalization of the electron density on the electron accepting cyanoacrylic group, a configuration favorable to charge injection thanks to the good overlap with the TiO₂ conduction band wavefunctions. This is clearly evident in the case of ZnB, where the short linker provides a strong coupling between the tetrapyrrolic ring and the anchoring group. ZnBT and ZnMT are characterized by a significant contribution of the dithienylethylene moiety, acting generally as a donor, to the lowest singlet excited states. The substantially planar ZnMT gives rise to long range CT states which display the strongest red shift, consistent with the experimental absorption spectra. The involvement of the amino donor group linked to the *meso* position opposite to the DTE group can be appreciated in transitions 1,4,5,7 whereas in transition 6 it is mostly the tetrapyrrolic ring which behaves as the electron donor. Such long range directionality of the first excited states is less pronounced in the ZnBT dye, probably due to both the twisting angle (27°) between the macrocycle and the electronic acceptor and the lack of the electron donating amino group. Thus, together with the porphyrin ring, it is often the DTE bridge which plays the prominent role as electron donor in charge transfer transitions. Interestingly, the EDDM of transition 7 (2.55 eV) in ZnBT points to a reversed direction of the CT state, where the

DTE arm acts as the donor and the porphyrin ring as the acceptor. Such electronic distribution would be unfavorable to fast charge injection, but relaxation to the lower charge transfer states 5, 4 and 1, having the appropriate directionality for charge injection, may occur on ultrafast timescales. For example, although internal conversion is considered to be slower in Zn porphyrins with respect to free base analogs, evidence for internal conversion in the hundred fs-ps time scale from the B to Q states of symmetric porphyrins has been reported in condensed phases.³⁹⁻⁴¹ Herein the population of a series of intermediate energy excited states having a sizable density on the electron acceptor may provide additional channels for fast deactivation to the lowest CT state.

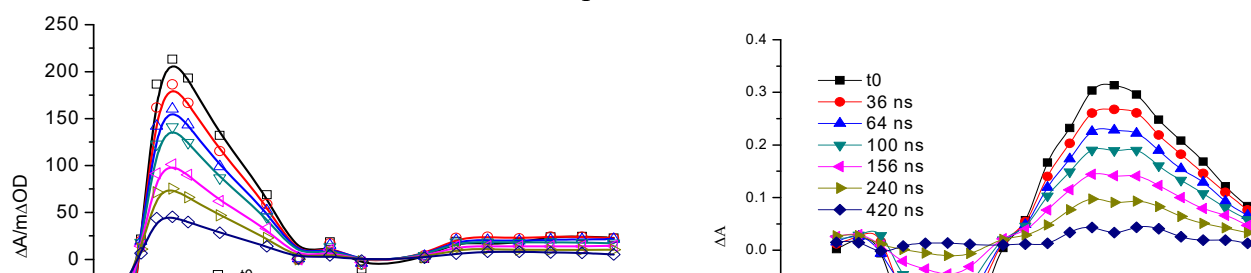
Thus, in all cases, population of the absorption manifold between the B and Q bands is expected to result in efficient charge injection, either because a CT state with appropriate directionality is directly generated, or because thermalization to the lowest excited states having in every case the correct spatial orientation would occur on time scales compatible with ultrafast charge injection into TiO₂.

The structural and electronic properties of the oxidized dye generated by charge injection are also important in determining the kinetics of electron recapture, with an impact on the ultimate efficiency of the dye in the solar device. Unrestricted DFT-6311 G,d calculations *in vacuo* carried out on mono-oxidized ZnB, ZnBT and ZnMT dyes (+1 charge, doublet state) showed no major structural changes following a single electron loss. Both ZnB and ZnMT preserved a substantial co-planarity of the conjugated linker with the tetrapyrrolic ring while the torsion of the ZnBT dye was also maintained in the oxidized state, although the twist was reduced to ca. 20°. In general the highest singly occupied molecular orbital (HSOMO) of all the dyes under investigation displays a rather delocalized nature, showing involvement of both the conjugated linker and of the macrocycle. The electronic coupling for charge recombination could be thus expected to be comparable.

Excited State Dynamics in solution

Nanosecond TA

Upon UV-Vis excitation, all dyes were found to be emissive in THF/EtOH solution, with a lifetime which is essentially constant within the explored series, equal to 1.6 ns and assigned to deactivation of the lowest singlet state (S1). The nanosecond excitation (7 ns FWHM) at 532 nm is resonant with the absorption manifold between the Q and B band of each dye. Long lived (hundred nanoseconds) ns-TA spectra were observed (Figure 3) assigned to population of their respective lowest triplet excited states (T1) occurring within the instrumental response of the apparatus. The triplet state decays monoexponentially in aerated solution with a lifetime of 550 ns for ZnB and of the order of 250 ns for the other two DTE substituted species.



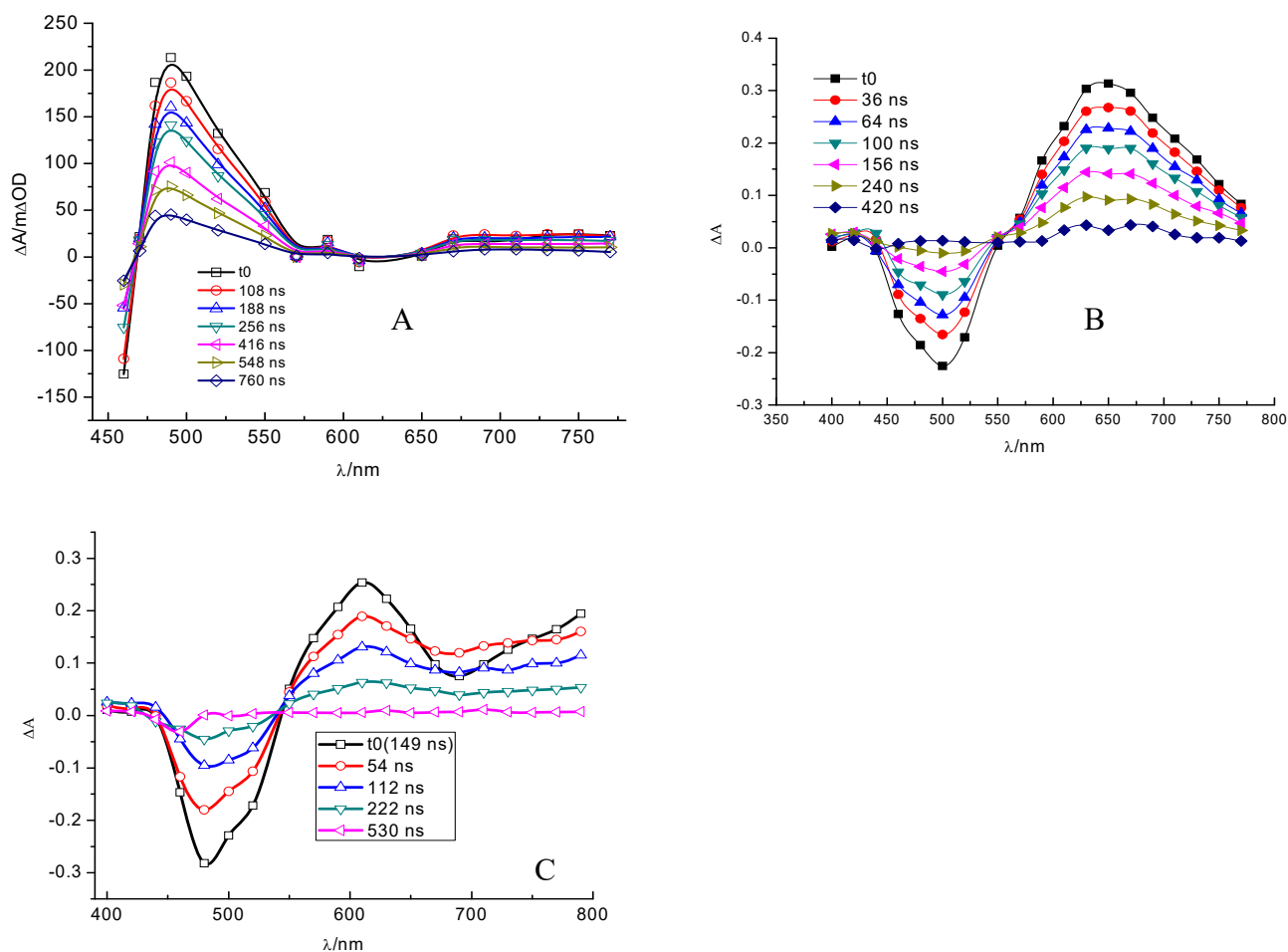


Figure 3. ns-TA spectrum of the porphyrin dyes in Ethanol/THF A) ZnB; (B) ZnBT; (C) ZnMT. Notice that fluorescence convolved with the laser excitation was avoided by choosing appropriate delays after the excitation ($t_0 > 100$ ns) and that at the concentrations used for these measurements (A_{532} ca. ≥ 0.5) the GSB of the B band was only partially evident due to the strong ground state absorption leading to the complete extinction of the probe light at $\lambda < 450$ nm.

The triplet state of ZnB in solution (Figure 3A) is characterized by features already observed in a previous contribution.²⁰ In particular, besides the ground state bleaching (GSB) of the B band, partly visible for $\lambda < 450$ nm, the triplet spectrum is dominated by an intense triangular shaped photoinduced absorption (PA) band centered at ca. 500 followed by the GSB of the Q band and by a comparatively weak and featureless PA band extended to the red.

The triplet state signatures of the β and *meso* DTE substituted dyes are similar among themselves, but they are very different from that of ZnB (Figure 3 B,C). These spectral fingerprints consist in a GSB band centered at 480-500 nm, which mirrors the ground state absorption due to the presence of transitions originated by mixed contributions of both the pyrrolic macrocycle and the π -conjugated DTE pendant. The GSB is followed, after a well-defined isosbestic point at ca. 550 nm, by an intense PA band in the red part of the spectrum. Consistent with the EDDMs 1 of both ZnMT and ZnBT, the

comparison with the TA spectrum of ZnB leads us to assign the strong PA band peaking at 610-630 nm to the triplet-triplet transitions from the T1 state having a sizable electronic density localized at the periphery of the DTE/cyanoacrylic group, confirming thus the charge transfer character conferred by the presence of the extended π conjugation.

Femtosecond TA .

The fs-TA spectra of ZnB following 480 nm excitation are shown in Figure 4. One can appreciate the formation of the singlet state characterized by the GSB of the B band (positive in band in $\Delta T/T$ mode) by the appearance of a broad PA band with maximum at 513 nm and of narrow absorption band at 603 nm. These spectral signatures, which rise within the instrumental response function (Figure 3S A and B) decay with a monoexponential time constant, probed at both 513 and 603 nm, of ca. 130 ps (Figure 4S) to a very long lived excited state, whose lifetime is constant for the available range of delays (up to ≈ 1 ns). Besides the B band GSB, this long lived state is characterized by a triangular shaped broad PA band peaking at 500 nm (Figure 5S), in good agreement with the results of the ns-TA experiment. The picosecond dynamics is therefore assigned to the formation of the triplet state of the dye, which predominantly characterizes the TA spectra at delays longer than 400 ps.

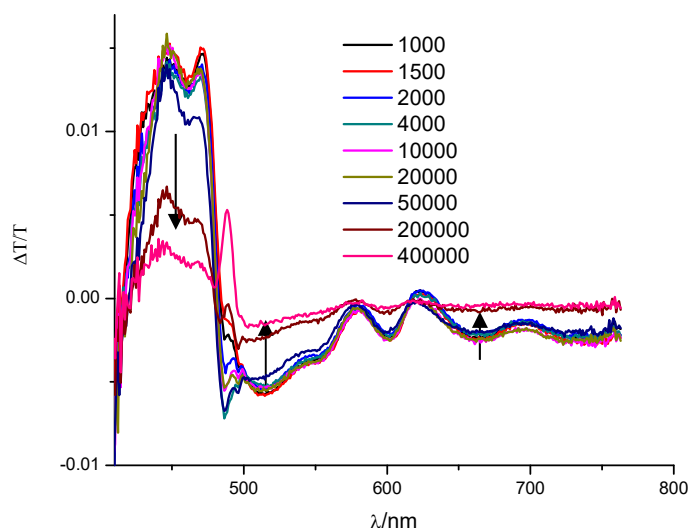


Figure 4. Picosecond time domain evolution of the transient spectrum of ZnB in ethanol/THF, following 480 nm excitation. Significant delays sampled along the excited state decay curve are reported to illustrate the major spectral changes occurring after excitation.

The fs-TA spectra of ZnBT following excitation of the 510 nm absorption manifold are shown in Figure 5. The kinetics are generally multi-exponential, due to the relaxation from higher lying electronic states centered on the conjugated bridge to the lowest singlet state having a prevalent HOMO-LUMO component. This process has fast kinetics, with a major component ($> 90\%$) on the

order of 600 fs, and a longer minor component (< 10%) with a lifetime of ca. 10 ps. This kinetics is particularly evident from the fast and clean growths of the 500 nm and 650 nm PA bands (Figure 6S and 7S). A further kinetic process having a lifetime on the order of hundreds ps contributes to the recovery of the 500 nm signal, which turns into a progressively increasing GSB. The 650 nm absorption also continues to grow with a similar time constant of xxx ps (Figure 7S). In general for delays larger than 400 ps the fs-TA spectrum acquires strong similarities with the triplet spectrum recorded by 532 nm nanosecond excitation, suggesting that intersystem crossing to the T1 state is the predominant dynamical process on the sub-nanosecond time scale (Figure 5B). Consistent with the ns- μ s results, the major spectral features of the T1 state are indeed the intense symmetric PA band at 650 nm and the well-defined GSB at 500 nm with the presence of the isosbestic point centered around 550 nm.

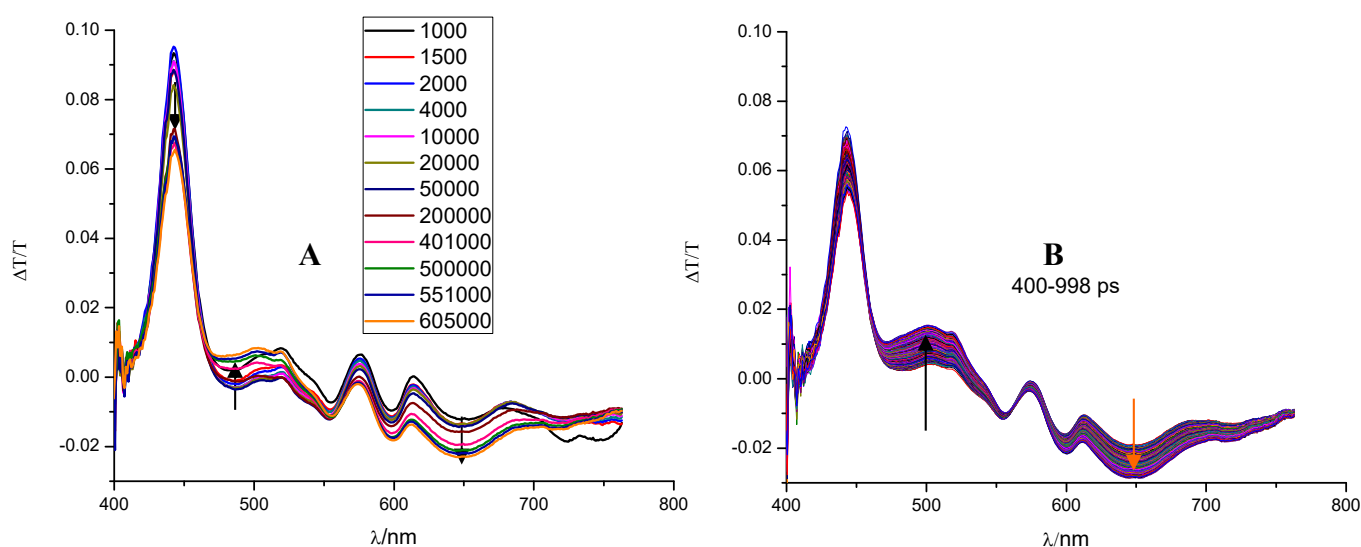


Figure 5. (A) Time evolution of the transient spectrum of ZnBT in ethanol/THF, following 510 nm excitation. Significant delays sampled along the excited state decay curve are reported to illustrate the major spectral changes occurring after excitation. (B) Excited state dynamics on the 400-1000 ps time scale, showing the deepening of the bleaching at 500 nm and the increase of the 650 nm band.

The fs-TA spectra of ZnMT upon 510 excitation (Figure 6) are characterized by an initially fast decay dynamics (Figure 8S) which is assigned to internal conversion from higher lying CT states populated by 510 nm excitation. There is a red shift of the 650 nm GSB (Q-band bleaching) which is achieved after ca. 1 ps after the initial pulse, due to the presence of stimulated emission (SE), resulting in a band peaking at 700 nm, which decreases as the singlet is progressively de-populated. In this case, the observation of a SE band in fs-TA spectroscopy is probably due the electric dipole of ZnMT, which, due to planarity and enhanced push-pull character, is expected to be the strongest among the explored series. This favors radiative deactivation compared to the other two cases. This initial

bleaching is partially offset by the slower growth of a low energy PA band and its evolution monitored at 664 nm continues according to a bi-exponential kinetics having a minor component (amplitude ca $\frac{1}{4}$) with a lifetime of 30 ps and a major component (amplitude ca. $\frac{3}{4}$) with a lifetime of ca. 400 ps. Such long lived state, whose spectral fingerprints do not change appreciably in the time window 400 ps/1 ns is characterized by the presence of a comparatively weak absorption at 700 nm, and by a well-defined absorption band centered at 600 nm, which progressively increases (Figure 9S). A bleaching band in the 510-530 nm region also becomes more defined, consistent with the band reported in Figure 3C. Overall these features suggest that population of the lowest triplet state is already significant after 200 ps following the initial excitation and that triplet is the dominant state contributing to absorption in the 400-1000 ps time frame.

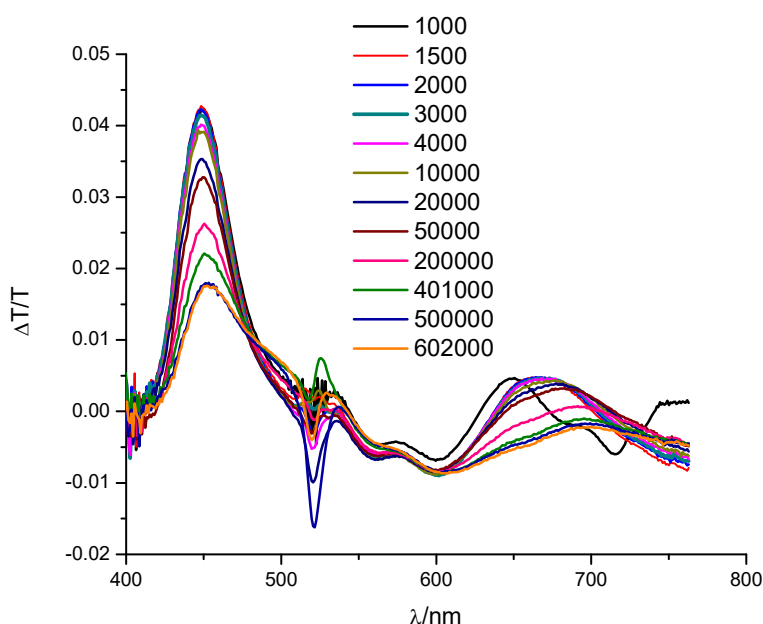


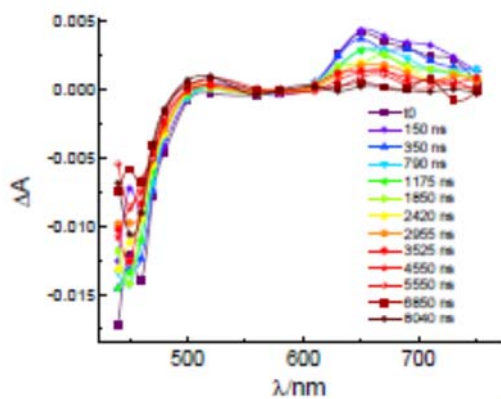
Figure 6. Time evolution of the fs-TA spectra of ZnMT in ethanol/THF, following 510 nm excitation. Significant delays sampled along the excited state decay curve are reported to illustrate the major spectral changes occurring after excitation.

3) Charge Transfer on TiO₂

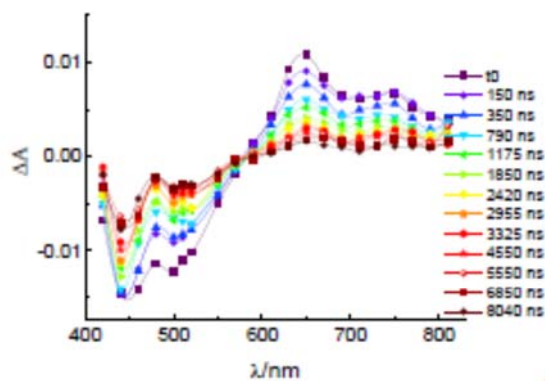
3.1 Charge Recombination and Dye Regeneration probed by ns- μ s spectroscopy

532 nm excitation of ZnB, ZnBT and ZnMT results in the instrumental response (ca. 10 ns) limited formation of a long-lived charge separated state ($\text{Dye}^+/\text{e}^-(\text{TiO}_2)$) having an average lifetime of ca. 7 μ s for ZnB, 14 μ s for ZnBT and 11 μ s for ZnMT, clearly much longer than the corresponding triplet states in aerated conditions (Figures 7 and 8). In all cases a residual amplitude, varying from 30 to 60% of the initial value, does not recover by electron recapture on a time scale varying between 10 to 20 μ s. The spectral fingerprints of ZnB^+ (Figure 7(a)) are summarized by the bleach of the ground

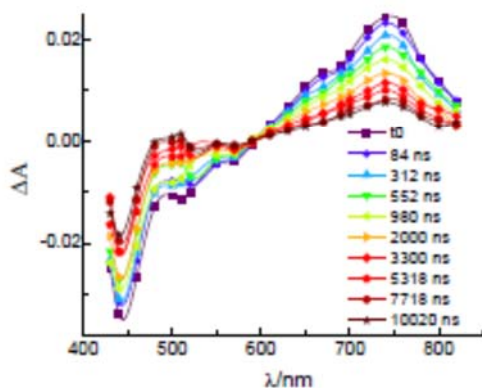
state, evident in correspondence of the sharp and intense B band at 450 nm, and by a low energy absorption rising for $\lambda > 650$ nm. The lack of the intense 500 nm absorption characterizing the triplet of ZnB allows to rule out important spectral contributions of its triplet state to the transient spectrum recorded on TiO₂ in the ns- μ s time scale, suggesting complete quenching of the excited state by electron transfer. In ZnBT (Figure 7b) the ground state bleaching involves the manifold of excitations concerning both the macrocycle and the conjugated DTE substituent (Figure 7b). The structured absorption appearing for $\lambda > 600$ nm, displaying a maximum at about 650 nm is also assigned to the signature of the dye cation formed on the TiO₂ surface, consistent with similar features observed in ZnB⁺. In the case of ZnBT loaded on TiO₂, there is some similarity between the triplet absorption spectrum observed in solution and the transient spectrum recorded on TiO₂. Nevertheless, on TiO₂, the presence of a structured bleaching at 450 and 510 nm and well-defined absorption shoulder at ca. 750 nm (Figure 7b), not evidenced in solution, are indicative, even at early delays, of the formation of the dye cation. The transient spectrum of ZnMT loaded on TiO₂ (Figure 7c) is similar to that of ZnBT, and is characterized by two bleaching bands at 450 and 510 nm, due to B band and mixed CT transitions bleaching, followed by a large structured absorption band peaking at 750 nm, preceded by a shoulder at 650 nm and by an isosbestic at 610 nm.



(a)



(b)



(c)

Figure 7 ns-TA spectra of ZnB (a), ZnBT (b), and ZnMT (c), absorbed on TiO₂, in contact with ACN/Li⁺, following 532 nm excitation

Lifetime of the charge separated state for the three species was substantially shortened in the presence of the electron donating electrolyte consisting of 0.6M PMII/0.1M LiI/0.05M TBP (Figure 8) resulting in the complete recovery of each dye within 10 μs thanks to electron transfer from iodide to the oxidized sensitizers. The kinetic competition between recombination and regeneration in the microsecond time scale is very favorable, leading to nearly quantitative and fully comparable regeneration efficiencies ($\eta = 91\%$ for ZnB, 96% for ZnBT and 92% for ZnMT).

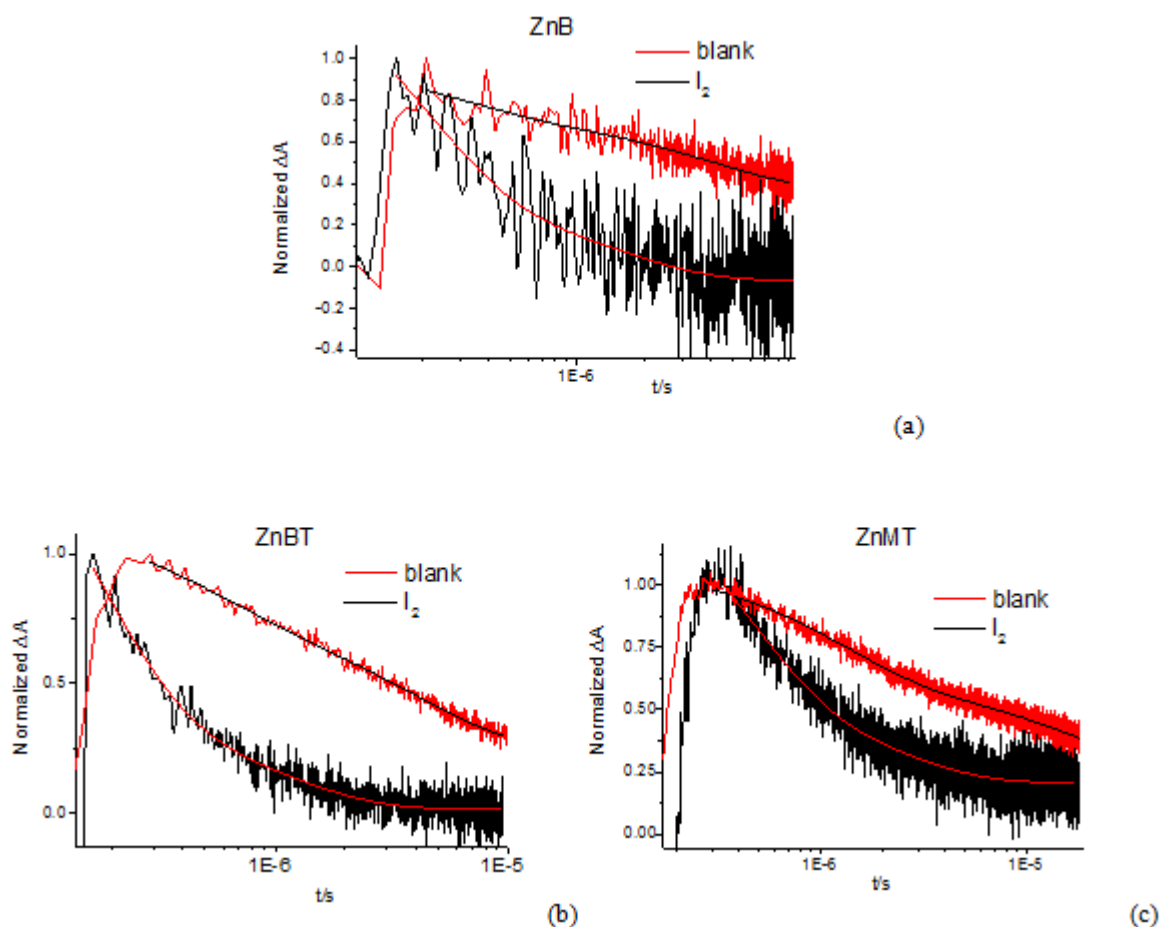


Figure 8 Recombination and regeneration kinetics observed on the ns-μs time scale., under 532 nm laser excitation (2.2 mJ/cm²/pulse), of ZnB (a), at 460 nm; of ZnBT (b), at 650 nm; of ZnMT (c), at 720 nm, fitted with bi-exponential functions. **Inoltre I2 non è appropriato, essendo la forma ossidata.**

Miglior I

3.2 Charge injection and recombination in the picosecond-subpicosecond time scale.

Charge injection studies on TiO₂ were mainly performed at 510 nm excitation wavelength, which excites the same absorption manifold of the dyes as the 532 nm wavelength used for nanosecond

studies. In general these excitation wavelengths populate the absorbing states which are found between the B band and the lowest lying Q bands. The fs-TA spectra of ZnB taken in the 1-4 ps time (Figure 9A) bear significant differences with respect to those recorded in solution at similar time scales (Figure 4A): at 600 nm there is a GSB instead of a PA band, while the long wavelength PA in the 630-700 nm region is less structured, and increases by moving into the red. The broad absorption band beginning at 600 nm resembles the one observed in the charge separated state ($\text{ZnB}^+/\text{e}^- (\text{TiO}_2)$) generated by nanosecond 532 nm excitation, suggesting that charge injection occurs on a time scale similar to the temporal width of the excitation pulse. This is also corroborated by the fact that the amplitude of the transient signal reaches its maximum intensity at very early delays, and maintains constant spectral features during the time evolution monitored up to 20 ps (Figure 9A), where the relative amplitudes of the TA spectra simply evolve according to a multi-exponential kinetics without modifying their shapes. To determine the dynamics of the charge injection process we monitored the TA dynamics at 615 nm (Fig. 11), which corresponds to an isosbestic point of the singlet excited state in solution, in order to avoid any interference from residual singlet excited state. We observe the build-up of a long-lived PA band, assigned to the charge separated state, with a rise time of 226 fs after deconvolution of the instrumental response function. This dynamics is essentially independent of the excitation wavelength (both 480 and 510 nm excitations yield similar rates of formation of the charge separated state). Similar conclusions can be drawn by observing the dynamics of the ZnBT and ZnMT dyes loaded on TiO_2 thin films. The formation of the charge separated state, consistent with the spectral features observed by nanosecond spectroscopy, is evident at very early delays after the fs excitation of the dye: ZnBT shows the immediate appearance of a broad low energy PA band preceded by the characteristic narrow 640 nm shoulder (Figure 10A). The GSB manifold is also structured with a narrow 450 nm shoulder (B band) followed by a broader 500 nm band, in agreement with those observed in ns-TA. The kinetic analysis at the 567 nm excited state isosbestic point of ZnBT (Figure 11B) confirms that the injection occurs during the first 250-300 fs showing a GSB partly convolved with the excitation pulse whose rise could be fitted with a Gaussian function having 170 fs FWHM. The *meso* substituted dye ZnMT has spectral features similar to those of ZnBT, consistent with previous ns- μs observations, with an intense low energy PA band reaching a maximum around 750 nm. The main two GSB bands at 450 and 500 nm are also similar to those of ZnBT (Figure 10B). SE was also not observed, confirming ultrafast quenching of the singlet state by charge injection. Similar to ZnBT, the 710 nm rise could be well fitted with a Gaussian having 217 fs FWHM (Figure 11 C).

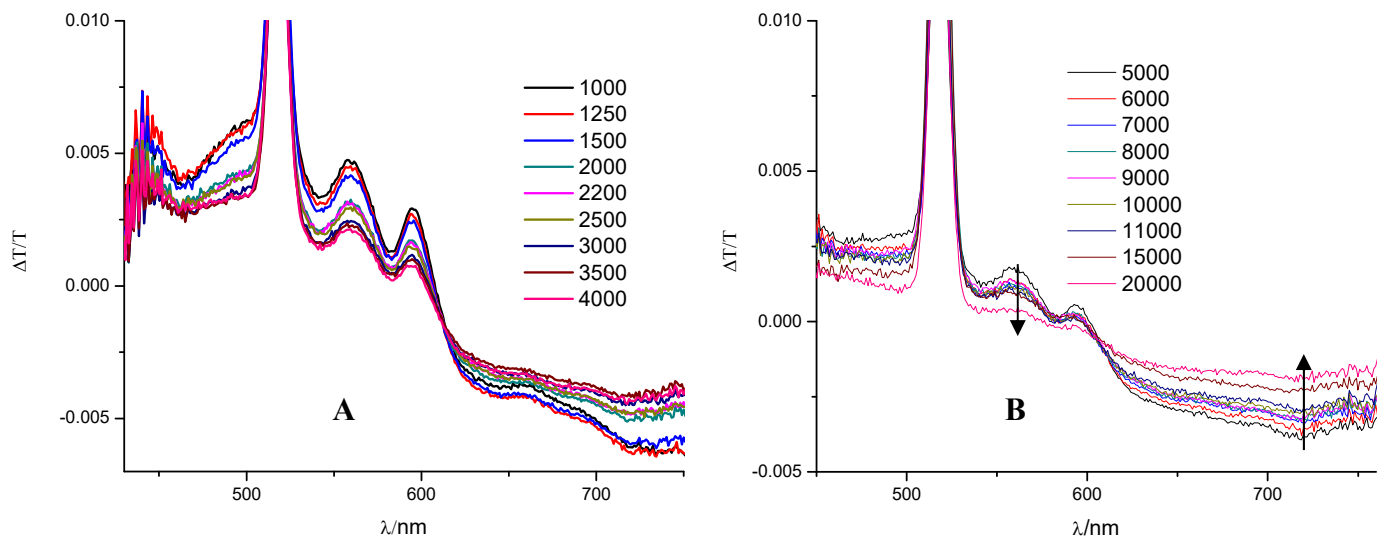


Figure 9. fs-TA spectrum of ZnB loaded on TiO₂ thin film following 510 nm excitation (A) early delays 1-4 ps; (B) late delays 5-20 ps. Early and late delays are reported in different figures for sake of clarity. Note that the region around 510 nm, which is affected by strong pump scattering, is removed from the spectra.

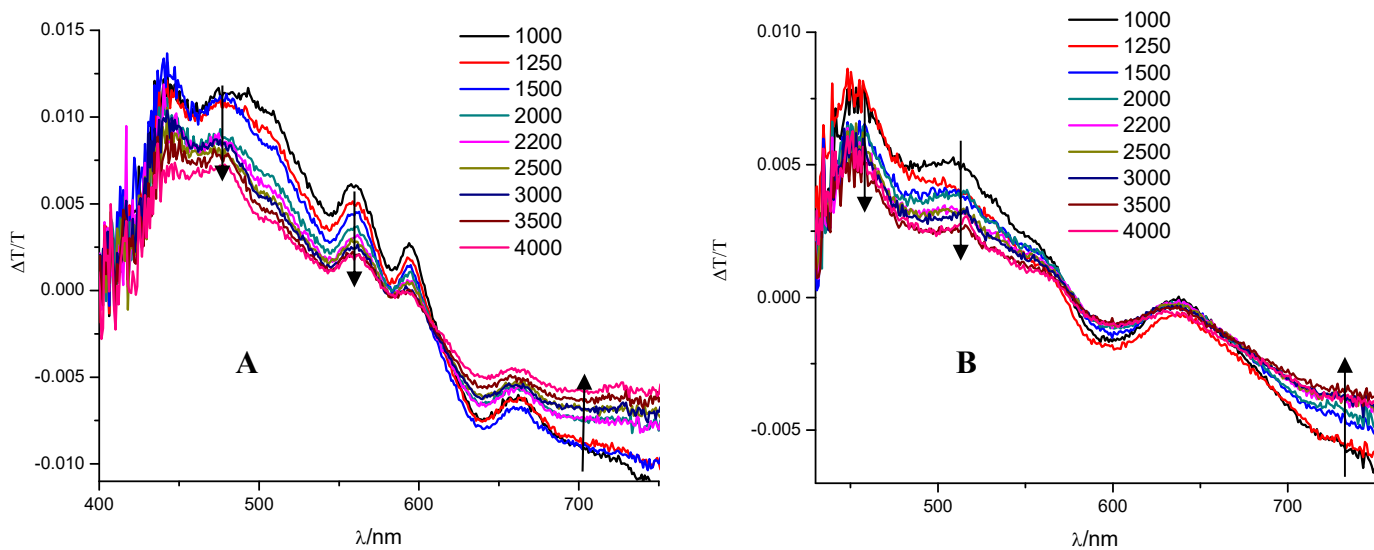


Figure 10. Transient spectra of ZnBT (A) and ZnMT (B) following 510 nm excitation observed framed up to 4 ps delay.

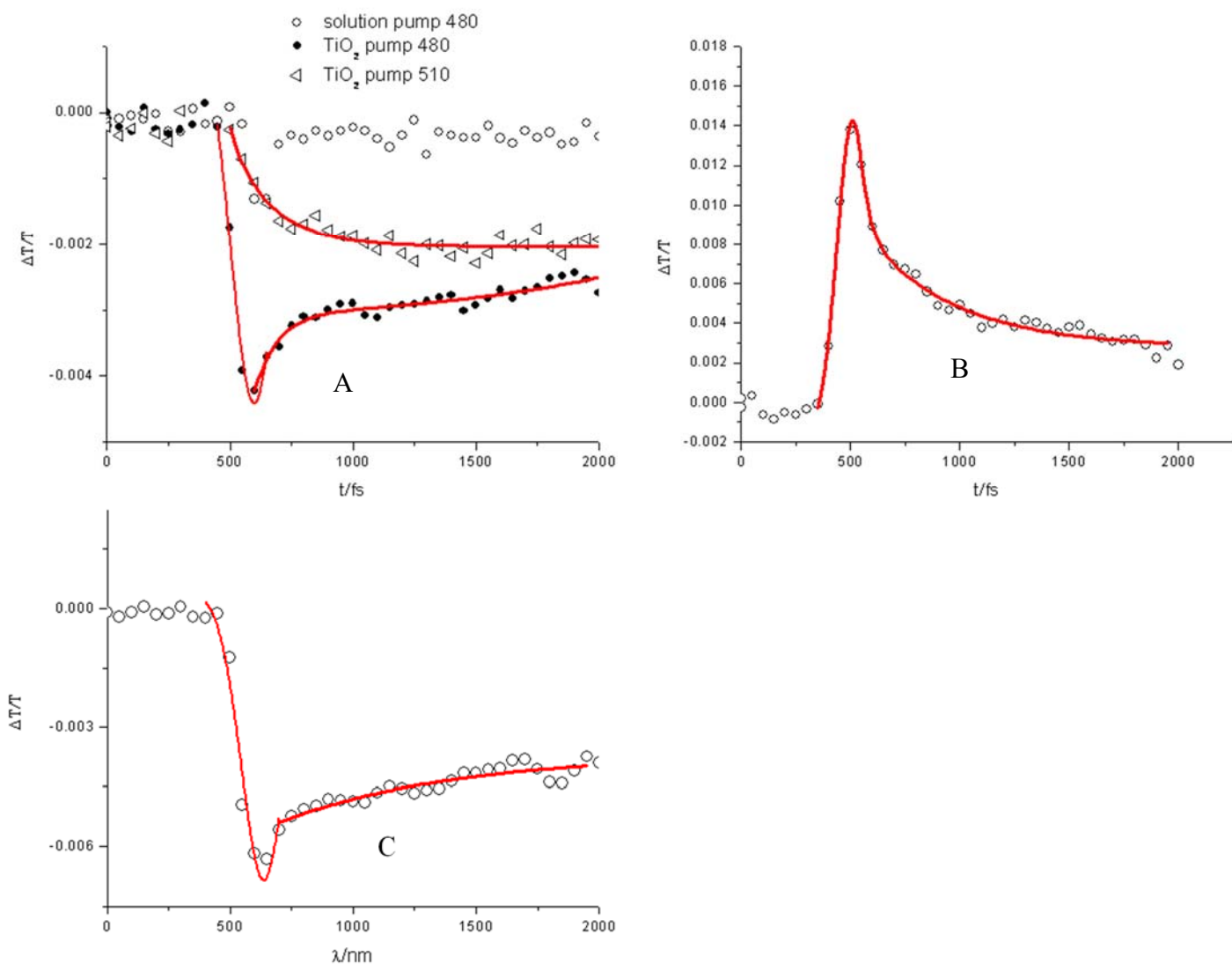


Figure 11. Injection kinetics into TiO₂ resulting in the formation of the oxidized dye: A) ZnB absorption observed at the excited state isosbestic point of 615 nm; B) ZnBT bleaching observed at the excited state isosbestic point of 567 nm ; C) ZnMT absorption observed at 710 nm.

The multiexponential recovery (Figure 11 and Figure 12) generally observed with all dyes after generation of the charge separated state is ascribed to initially fast charge recombination. In general, the decay up to 20 ps can be well fitted by a biexponential function whose average lifetime varies in the order ZnBT (1.8 ps) < ZnMT (3.8 ps) < ZnB (5.3 ps). In all cases a long lived state is approached after ca. 5 ps, whose amplitude varies from ca. 1/2 (ZnB) to ca. 1/3 (ZnBT and ZnMT) of the initial signal. Such long lived component of the cationic state is then capable of surviving well beyond the microsecond time scale, as observed by ns- μ s spectroscopy. Compared to ZnB, the presence of more rapid recombination kinetics found in dyes conjugated with the DTE pendant suggests that, in these cases, a smaller fraction of the oxidized dye is able to survive initially fast electron recapture, on a timescale where dye regeneration by bi-molecular events involving the redox couple cannot occur.

This fast recombination could be a consequence of the experimental conditions adopted in the fs-TA experiment, due to the high density of photoexcitations generated by the 70 fs pump pulse, possibly resulting in geminate recombination. Nevertheless ultrafast pump-probe photoinjection studies involving well-known Ru(II) complexes, like [Ru(II)(bpy)₂(NCS)₂], did not show a fast recombination component involving Ru(III) and photoinjected electrons.^{28, 42} This suggests that electron recombination on fast time scales could be a limiting factor in the efficiency of highly conjugated porphyrin sensitizers, having push-pull characteristics, particularly under strong irradiance conditions. This is consistent with observations by Griffith *et al.*⁴³ who, when analyzing a series of β and *meso* substituted porphyrins, encountered in some cases a fast recombination dynamics on the ps-ns time scale. Evidences of ps and sub-ps recombination processes involving push-pull organic dye sensitizers has been provided by Wiberg *et al.*,⁴⁴ while a fast recombination component in different Zn-porphyrins equipped with π conjugated linkers having various lengths was observed by the Diao group.⁴⁵ Interestingly, as also observed by us, they found a larger amplitude of the fast recombination component in the porphyrin dye equipped with the longer conjugated linker chains (3.3 nm) with respect the shorter one (1.2 nm). Such evidence was explained by tilting of the longer dyes on the TiO₂ surface, and by through space, rather than through bond, recombination pathways involving adjacent TiO₂ nanoparticles, which, in the highly disordered nanocrystalline film, are able to couple more efficiently with longer dye molecules, providing additional channels for fast recombination.

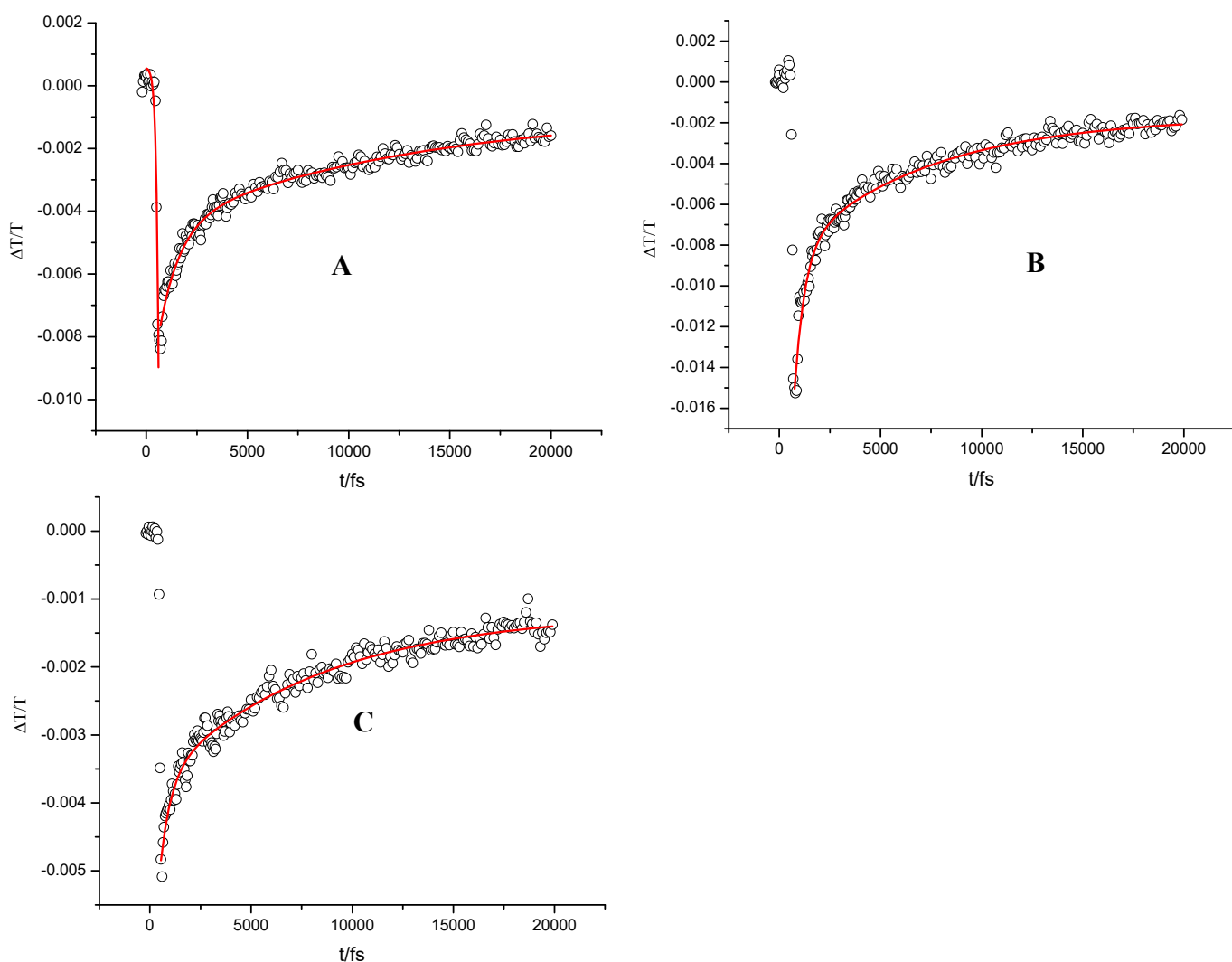


Figure 12. Generation and decay of the charge separated state of porphyrin dyes on TiO_2 thin films within the time frame of 20 ps fitted with bi-exponential functions. (A) ZnB observed at 750 nm; (B) ZnBT observed at 750 nm (C) ZnMT observed at 700 nm.

Photoelectrochemistry in sandwich DSSCs.

The time-resolved spectroscopic investigations shed light on the fundamental processes of charge separation, charge recombination and dye regeneration occurring at this type of porphyrin sensitized TiO_2 interface. The essential results of such investigation are the following. 1) charge injection occurs on a time scale close to the temporal resolution of the fs-TA apparatus (170-220 fs). This, coupled with the ns lifetime of the singlet state of the porphyrins should provide quantum yield of charge injection close to unity. 2) Part of the charge recombination occurs on a fast time scale, leading to the loss of a sizable fraction of injected electrons which could limit the performance of the sensitized

solar cells; 3) the long lived component of the oxidized dye survives on the tens of microsecond time scale, enough for being regenerated with > 90 % efficiency by the iodide based electrolyte.

Photoelectrochemical investigations, and in particular IPCE measurements, are useful to evaluate the impact of the fundamental processes 1-3, occurring on a time scale spanning 7 orders of magnitude, on the operational device. In particular, we would like to emphasize that the evidence of sub-picosecond electron transfer does not automatically imply unitary quantum yield of charge injection: due to extreme surface heterogeneity of mesoscopic films, ultrafast injection accompanied by quantum yields <1 has been reported in some porphyrin sensitizers.⁴³ In our case the survival of a minor fraction of excited state (probably up to 20%) not quenched by charge transfer on ultrafast time scales would be difficult to rule out. This is due to the fact that, despite the presence of diagnostic fingerprints, both the excited state and the charge separated state contribute to absorption in the visible region. It is also not certain to what extent the presence of a population of oxidized dye which, under the pump fluences used in a ns-TA experiment, recombines on the ps time scale would affect the performance of the solar cell normally operating under either low or natural (i.e. 1 sun) illumination conditions.

Photoanodes for solar cells, fabricated with 3.5-micron-thick semi-opaque TiO₂, were sensitized by immersion in 0.2 mM solution of each dye, containing 0.2 mM CDCA. In the attempt to optimize dye performance solution composition and soaking time were varied as follows: ZnB (EtOH/THF 9:1, 2 h soaking); ZnBT (EtOH/THF 8:2, 5 h soaking) and ZnMT (EtOH/THF 9:1, 5 h soaking). In fact, DTE substituted dyes usually need a longer time to achieve surface saturation, probably due to their higher steric hindrance compared to ZnB. IPCE spectra of DSSCs were recorded in open configuration (i.e. cells not thermally sealed) (Figure 13) in order to avoid thermal stress to the sensitizers.

Photoaction spectra clearly show that the two porphyrins featuring the DTE unit, ZnBT and ZnMT, irrespective of their substitution pattern (β or *meso*), are able to produce a panchromatic response (Figure 13) over a wide range of wavelengths, from 400 to 700 nm. Conversely the IPCE of ZnB porphyrin, lacking of the thienyl acceptor unit, displays a slightly better conversion in the UV-Vis between 400 and 450 nm but poor efficiency (<40%) in the range of 500-550 nm and completely misses of response moving toward the NIR region (>650 nm).

The IPCE maximum values around 460 nm (B band) are close to 90% in all three cases (corrected for the FTO transmission). Interestingly, consistent with the spectroscopic investigation, the charge transfer states originated by the π -conjugated thienyl bridge, responsible for the absorption between 500 and 550 nm, are highly active in the conversion of photons to electrons, resulting in the broad feature characterizing the photoaction of the ZnBT and ZnMT dyes. This supports injection quantum

yields and regeneration efficiencies close to unity, at least under low-intensity monochromatic excitation. As expected, ZnMT generates photon to current conversions exceeding 700 nm in accordance with its small HOMO-LUMO gap. It is also noteworthy that ZnBT, despite its β -substitution pattern, upon sensitizing the semiconductor, produces a red responsivity profile very similar to the *meso* substituted ZnMT.

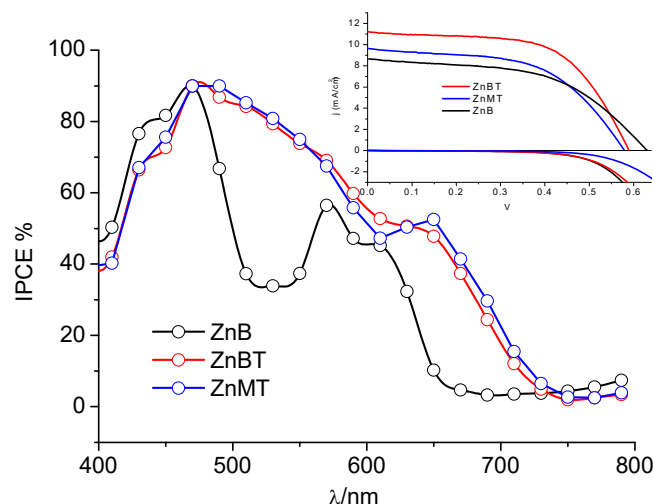


Figure 13: IPCE spectra of DSSCs based on semi-opaque TiO₂ (3.5 μ m) in the presence of 0.6 M PMII/ 0.1 M LiI/ 0.02 M I₂/0.05M Tbpv in ACN. Inset: JV curves of the same cells under AM 1.5 G.

Table 3. Efficiency Parameters of porphyrins based DSSC.

	J_{sc}	V_{oc}	FF	η %
ZnB	8.66	0.63	0.52	2.83
ZnBT	11.24	0.59	0.60	3.96
ZnMT	9.64	0.58	0.54	3.02

The JV curves recorded under simulated solar illumination are consistent with the IPCE, with the average photocurrents aligned around 10 mA/cm², with the ZnMT and ZnBT dyes showing, in some cases, a significantly larger photocurrent, as already reported for similar porphyrin systems²⁴ confirming the combination of better harvesting and comparable charge injection rates with respect to ZnB. Under AM 1.5 G, ZnBT is the best performing dye (Table 3) and, in hot press sealed cells, where the reduced electrode spacing and a temperature of ca. 80°C allows the electrolyte to achieve a better permeation of the TiO₂ film, it is able to achieve photocurrents of the order of 15 mA/cm² (Figure 10S). However, while ZnB generally produces sets of cells having a good reproducibility, highlighted by small error bars, ZnMT and ZnBT show a much greater dispersion, (Figure 11S) suggesting that the presence of the elongated pendant impacts on the adsorption conditions during cell fabrication and makes it more difficult to achieve cell optimization. This might be due to the larger steric hindrance of the long alkyl chains in the DTE unit, which produces variable dye loading

on the TiO₂ surface.

Interestingly ZnB, despite generating the lowest photocurrent, produces, under solar illumination, the best photovoltage (0.63 V vs 0.52 and 0.54 V of the other two DTE decorated dyes) in the explored conditions. This might be consistent with the observation of a larger fraction of oxidized ZnB which is able to survive fast recombination. We indeed expect this process to be more relevant under white light illumination and close to open circuit conditions, when the electronic population inside TiO₂ increases with respect to short circuit conditions. A substantial kinetic competition between electron recapture and dye regeneration has been indeed observed, at potentials corresponding to the maximum power point of the cell, by Meyer and co-workers.⁴⁶

Conversely, dark currents due to recombination involving I₃⁻ are, up to -0.55 V, fully comparable within the explored series (Figure 11S_da modificare), consistent with the expected shielding of the surface by these highly sterically crowded dyes.

We can thus confirm that the presence of the additional DTE chromophore introduces a panchromatic effect to both the ZnBT and ZnMT dyes resulting in a significant improvement of the photon to electron conversion both in the range from 500 nm to 550 nm and over 600 nm.

In particular ZnBT, despite the need for a careful tuning of the adsorption conditions, couples a reasonably straightforward synthetic route to the potential for improved energy conversion over existing β substituted structures.

CONCLUSION

In this work, we have comparatively investigated the three structurally different porphyrin dyes ZnB, ZnBT and ZnMT, designed for TiO₂ sensitization, with the aim of elucidating their excited state and electron transfer dynamics relevant to solar cell operation. ZnB is a tetraporphyrin substituted in β -position with a typical ethynylphenyl cyanoacrylic pendant, ZnBT shows a π -conjugated DTE unit as acceptor in β -position while ZnMT features a *meso* substitution pattern bearing the DTE unit as acceptor as well. The additional DTE chromophore confers panchromatic absorption characteristics to both ZnBT and ZnMT, due to the presence of CT states involving both the conjugated DTE bridge and the tetrapyrrolic macrocycle. The excitation of the dyes in the absorption manifold between the B and Q bands populates CT states which undergo internal conversion to the lowest singlet state excited state (S1) with time constants ranging from the sub-picosecond (major) to 10 ps (minor). The lowest singlet states decays according to a monoexponential kinetics with a lifetime of 1.6 ns. Population of the lowest triplet state (T1) proceeds at the sub-ns time scale, with intersystem crossing time constant ranging from 130 ps (ZnB) to ca. 400 ps (ZnMT, ZnBT). The triplet state survives for several hundred ns in aerated solution but is not involved in electron injection. The excited state

deactivation dynamic shares common features within the explored series which can be schematized below.

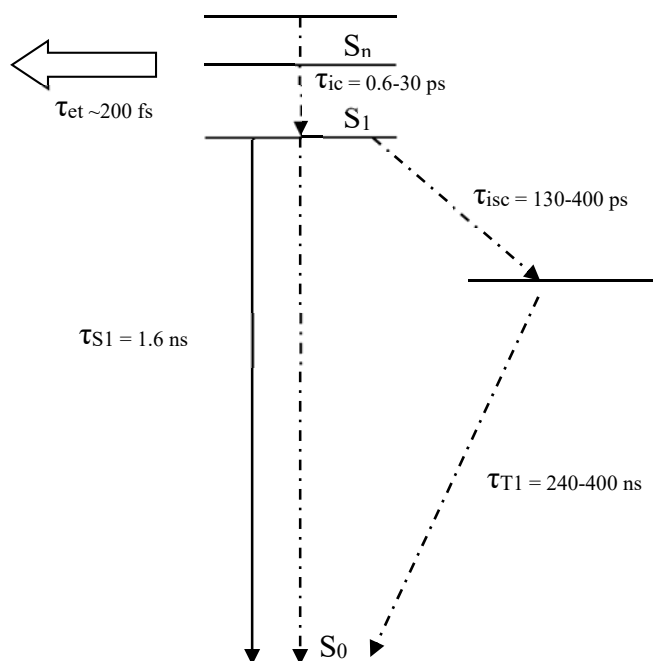


Figure 14. Schematic energy levels and deactivation time constant for the processes leading to deactivation of the excited states.

Excitation of the CT manifold bearing contributions by the DTE moiety results indeed in electron injection into the TiO_2 on a time scale of ca. 200 fs, suggesting nearly quantitative deactivation of the singlet states by electron transfer. The electron transfer kinetics is very similar to that of ZnB which, however, bears a much shorter acceptor arm.

The charge separated state on TiO_2 partly recombines according to a fast electron recapture kinetics in the ps timescale, while another fraction of the dye-cation population survives well beyond the microsecond time scale (recovery by charge recombination was in this latter case incomplete on a time scale of 2×10^{-5} s).

The observation of a ps-ns recapture kinetics is consistent with reports from other authors about the charge recombination dynamics in organic push-pull sensitizers, including different types of conjugated porphyrins, but could be exacerbated by the extreme power density achieved in the fs-TA experiment.

On the other hand, the long-lived fraction of the photogenerated oxidized dye can be nearly quantitatively intercepted by iodide, resulting to regeneration efficiencies approaching unity (97% for ZnBT, 90% for ZnMT and 92% for ZnB, at short circuit). Consistent with such photophysical observations, under low intensity monochromatic excitation, typical of IPCE measurements, quantum

yields approaching 80 % were observed with the DTE decorated dyes within the 500-550 nm spectral region, where the absorption of more common porphyrin designs would display poor harvesting and conversion. This is a confirmation that $\eta_{\text{collection}} \times \Phi_{\text{inj}}$ approaches unity in both the ZnMT and ZnBT species. Nevertheless, fast recombination between photoinjected electrons and oxidized porphyrin may be a limitation to cell efficiency under intense illumination and far from short circuit conditions, where the electron population inside the TiO₂ becomes more significant.

Finally, we could not observe any significant impact of the substitution position (either β or *meso*) on the elementary electron transfer kinetics which comprise charge injection, dye regeneration and charge recombination. A very long conjugated arm may however result in the activation of a channel of fast charge recombination, due to through space back electron transfer involving adjacent nanoparticles in the mesoscopic film. In the case of the DTE based conjugated linker, this potential drawback is more than compensated by extended spectral sensitization and efficient injection by panchromatic states.

It can be thus concluded that the structural modification of a porphyrin by adding an additional chromophore in either β or *meso* position has met the goal of extending the spectral response of the chromophore without introducing a kinetic barrier to charge injection and/or dye regeneration. Under this respect, β substitution is a promising strategy for achieving this result at the price of a reasonable synthetic complexity.

REFERENCES

1. R. R. King, D. C. Law, K. M. Edmondson, C. M. Fetzer, G. S. Kinsey, H. Yoon, R. A. Sherif and N. H. Karam, *Applied Physics Letters*, 2007, **90**, 183516.
2. C. Battaglia, A. Cuevas and S. De Wolf, *Energy & Environmental Science*, 2016, **9**, 1552-1576.
3. M. A. Green, A. Ho-Baillie and H. J. Snaith, *Nat Photon*, 2014, **8**, 506-514.
4. S. Günes, H. Neugebauer and N. S. Sariciftci, *Chemical Reviews*, 2007, **107**, 1324-1338.
5. D. Joly, L. Pelleja, S. Narbey, F. Oswald, T. Meyer, Y. Kervella, P. Maldivi, J. N. Clifford, E. Palomares and R. Demadrille, *Energy & Environmental Science*, 2015, **8**, 2010-2018.
6. B. O'Regan and M. Grätzel, *Nature*, 1991, **353**, 737-740.
7. S. Mathew, A. Yella, P. Gao, R. Humphry-Baker, F. E. Curchod, N. Ashari-Astani, I. Tavernelli, U. Rothlisberger, K. Nazeeruddin, M. D. and M. Grätzel, *Nat Chem*, 2014, **6**, 242-247.
8. Y.-C. Liu, H.-H. Chou, F.-Y. Ho, H.-J. Wei, T.-C. Wei and C.-Y. Yeh, *Journal of Materials Chemistry A*, 2016, **4**, 11878-11887.
9. W. M. Campbell, A. K. Burrell, D. L. Officer and K. W. Jolley, *Coordination Chemistry Reviews*, 2004, **248**, 1363-1379.
10. A. Fermi, M. Locritani, G. Di Carlo, M. Pizzotti, S. Caramori, Y. Yu, B. A. Korgel, G. Bergamini and P. Ceroni, *Faraday Discussions*, 2015, **185**, 481-495.
11. P. R. Mussini, A. Orbelli, F. Tessore, M. Pizzotti, C. Biaggi, G. Di Carlo, M. G. Lobello and F. De Angelis, *Electrochimica Acta*, 2012, **85**, 509-523.

12. C.-F. Lo, S.-J. Hsu, C.-L. Wang, Y.-H. Cheng, H.-P. Lu, E. W.-G. Diau and C.-Y. Lin, *The Journal of Physical Chemistry C*, 2010, **114**, 12018-12023.
13. W. M. Campbell, K. W. Jolley, P. Wagner, K. Wagner, P. J. Walsh, K. C. Gordon, L. Schmidt-Mende, M. K. Nazeeruddin, Q. Wang, M. Grätzel and D. L. Officer, *The Journal of Physical Chemistry C*, 2007, **111**, 11760-11762.
14. A. Yella, H.-W. Lee, H. N. Tsao, C. Yi, A. K. Chandiran, M. K. Nazeeruddin, E. W.-G. Diau, C.-Y. Yeh, S. M. Zakeeruddin and M. Grätzel, *Science*, 2011, **334**, 629-634.
15. T. Bessho, S. M. Zakeeruddin, C.-Y. Yeh, E. W.-G. Diau and M. Grätzel, *Angewandte Chemie International Edition*, 2010, **49**, 6646-6649.
16. C.-W. Lee, H.-P. Lu, C.-M. Lan, Y.-L. Huang, Y.-R. Liang, W.-N. Yen, Y.-C. Liu, Y.-S. Lin, E. W.-G. Diau and C.-Y. Yeh, *Chemistry – A European Journal*, 2009, **15**, 1403-1412.
17. A. Covezzi, A. Orbelli Biroli, F. Tessore, A. Forni, D. Marinotto, P. Biagini, G. Di Carlo and M. Pizzotti, *Chemical Communications*, 2016, **52**, 12642-12645.
18. G. Magnano, D. Marinotto, M. P. Cipolla, V. Trifiletti, A. Listorti, P. R. Mussini, G. Di Carlo, F. Tessore, M. Manca, A. Orbelli Biroli and M. Pizzotti, *Physical Chemistry Chemical Physics*, 2016, **18**, 9577-9585.
19. K. Chaitanya, X.-H. Ju and B. M. Heron, *RSC Advances*, 2014, **4**, 26621-26634.
20. G. Di Carlo, S. Caramori, V. Trifiletti, R. Giannuzzi, L. De Marco, M. Pizzotti, A. Orbelli Biroli, F. Tessore, R. Argazzi and C. A. Bignozzi, *ACS Applied Materials & Interfaces*, 2014, **6**, 15841-15852.
21. G. Di Carlo, A. Orbelli Biroli, M. Pizzotti, F. Tessore, V. Trifiletti, R. Ruffo, A. Abboto, A. Amat, F. De Angelis and P. R. Mussini, *Chemistry – A European Journal*, 2013, **19**, 10723-10740.
22. A. Orbelli Biroli, F. Tessore, M. Pizzotti, C. Biaggi, R. Ugo, S. Caramori, A. Aliprandi, C. A. Bignozzi, F. De Angelis, G. Giorgi, E. Licandro and E. Longhi, *The Journal of Physical Chemistry C*, 2011, **115**, 23170-23182.
23. G. Di Carlo, A. Orbelli Biroli, F. Tessore, M. Pizzotti, P. R. Mussini, A. Amat, F. De Angelis, A. Abboto, V. Trifiletti and R. Ruffo, *The Journal of Physical Chemistry C*, 2014, **118**, 7307-7320.
24. E. M. Barea, R. Caballero, L. López-Arroyo, A. Guerrero, P. de la Cruz, F. Langa and J. Bisquert, *ChemPhysChem*, 2011, **12**, 961-965.
25. S. Arrechea, J. N. Clifford, L. Pellejà, A. Aljarilla, P. de la Cruz, E. Palomares and F. Langa, *Dyes and Pigments*, 2016, **126**, 147-153.
26. K. Sunahara, A. Furube, R. Katoh, S. Mori, M. J. Griffith, G. G. Wallace, P. Wagner, D. L. Officer and A. J. Mozer, *The Journal of Physical Chemistry C*, 2011, **115**, 22084-22088.
27. S. E. Koops, B. C. O'Regan, P. R. F. Barnes and J. R. Durrant, *Journal of the American Chemical Society*, 2009, **131**, 4808-4818.
28. Y. Tachibana, S. A. Haque, I. P. Mercer, J. R. Durrant and D. R. Klug, *The Journal of Physical Chemistry B*, 2000, **104**, 1198-1205.
29. M. J. Frisch, G. W. Trucks, H. B. Schlegel, G. E. Scuseria, M. A. Robb, J. R. Cheeseman, G. Scalmani, V. Barone, B. Mennucci, G. A. Petersson, H. Nakatsuji, M. Caricato, X. Li, H. P. Hratchian, A. F. Izmaylov, J. Bloino, G. Zheng, J. L. Sonnenberg, M. Hada, M. Ehara, K. Toyota, R. Fukuda, J. Hasegawa, M. Ishida, T. Nakajima, Y. Honda, O. Kitao, H. Nakai, T. Vreven, J. A. Montgomery, J. E. Peralta, F. Ogliaro, M. Bearpark, J. J. Heyd, E. Brothers, K. N. Kudin, V. N. Staroverov, R. Kobayashi, J. Normand, K. Raghavachari, A. Rendell, J. C. Burant, S. S. Iyengar, J. Tomasi, M. Cossi, N. Rega, J. M. Millam, M. Klene, J. E. Knox, J. B. Cross, V. Bakken, C. Adamo, J. Jaramillo, R. Gomperts, R. E. Stratmann, O. Yazyev, A. J. Austin, R. Cammi, C. Pomelli, J. W. Ochterski, R. L. Martin, K. Morokuma, V. G. Zakrzewski, G. A. Voth, P. Salvador, J. J. Dannenberg, S. Dapprich, A. D. Daniels, O. Farkas, J. B. Foresman, J. V. Ortiz, J. Cioslowski and D. J. Fox, *Gaussian 09, Revision D.01*, Gaussian, Inc., Wallingford CT, 2013.

30. A. D. Becke, *The Journal of Chemical Physics*, 1993, **98**, 5648-5652.
31. C. Lee, W. Yang and R. G. Parr, *Physical Review B*, 1988, **37**, 785-789.
32. B. Miehlich, A. Savin, H. Stoll and H. Preuss, *Chemical Physics Letters*, 1989, **157**, 200-206.
33. M. Cossi, N. Rega, G. Scalmani and V. Barone, *Journal of Computational Chemistry*, 2003, **24**, 669-681.
34. A. J. Bard and L. R. Faulkner, eds., *Electrochemical Methods. Fundamentals and Applications.*, Wiley, New York, 2002.
35. G. Gritzner, *pac*, 1990, **62**, 1839-1858.
36. G. Gritzner and J. Kuta, *pac*, 1984, **56**, 461-466.
37. M. Mba, M. D'Acunzo, P. Salice, T. Carofiglio, M. Maggini, S. Caramori, A. Campana, A. Aliprandi, R. Argazzi, S. Carli and C. A. Bignozzi, *The Journal of Physical Chemistry C*, 2013, **117**, 19885-19896.
38. T. Amaya, Y. Shimizu, Y. Yakushi, Y. Nishina and T. Hirao, *Tetrahedron Letters*, 2010, **51**, 2416-2419.
39. S. Akimoto, T. Yamazaki, I. Yamazaki and A. Osuka, *Chemical Physics Letters*, 1999, **309**, 177-182.
40. N. Mataga, Y. Shibata, H. Chosrowjan, N. Yoshida and A. Osuka, *The Journal of Physical Chemistry B*, 2000, **104**, 4001-4004.
41. H.-Z. Yu, J. S. Baskin and A. H. Zewail, *The Journal of Physical Chemistry A*, 2002, **106**, 9845-9854.
42. Y. Tachibana, J. E. Moser, M. Grätzel, D. R. Klug and J. R. Durrant, *The Journal of Physical Chemistry*, 1996, **100**, 20056-20062.
43. M. J. Griffith, K. Sunahara, P. Wagner, K. Wagner, G. G. Wallace, D. L. Officer, A. Furube, R. Katoh, S. Mori and A. J. Mozer, *Chemical Communications*, 2012, **48**, 4145-4162.
44. J. Wiberg, T. Marinado, D. P. Hagberg, L. Sun, A. Hagfeldt and B. Albinsson, *The Journal of Physical Chemistry C*, 2009, **113**, 3881-3886.
45. C.-W. Chang, L. Luo, C.-K. Chou, C.-F. Lo, C.-Y. Lin, C.-S. Hung, Y.-P. Lee and E. W.-G. Diau, *The Journal of Physical Chemistry C*, 2009, **113**, 11524-11531.
46. K. C. D. Robson, K. Hu, G. J. Meyer and C. P. Berlinguette, *Journal of the American Chemical Society*, 2013, **135**, 1961-1971.

Graphical abstract

